THERMO-MECHANICAL BEHAVIOR OF LITHIUM-ION BATTERY

ELECTRODES

A Thesis

by

KAI AN

Submitted to the Office of Graduate and Professional Studies of
Texas A&M University
in partial fulfillment of the requirements for the degree of

MASTER OF SCIENCE

Chair of Committee,   Partha P. Mukherjee
Committee Members,   Debjyoti Banerjee
                        Yalchin Efendiev
Head of Department,   Andreas A. Polycarpou

December 2013

Major Subject: Mechanical Engineering

ABSTRACT

Developing electric vehicles is widely considered as a direct approach to resolve the energy and environmental challenges faced by the human race. As one of the most promising power solutions to electric cars, the lithium ion battery is expected to achieve better performance, durability and safety. Fracture induced by lithiation and deliathiation stress has been identified as a major mechanism that leads to capacity loss and performance degradation.

This work aims to shed light on the thermo-mechanical behavior of lithium ion battery electrodes. It presents a single particle model of random lattice spring elements coupled with solid phase Li-ion diffusion under active temperature effects. The thermal features are realized by solving a lumped heat conduction equation and by including temperature dependent parameters. This model combined with a typical equivalent-circuit model is used to predict the impedance response of electrode particles.

The fracture generation increases as the temperature decreases. However, the diffusion induced fracture is found to be proportional to the current density and particle sizes. Simulations under realistic driving conditions show that the fraction of particle damage is determined by the highest current density drawn from the battery. A 3D phase map of fracture damage is presented.

The transit fracture growing process reveals a saturation phenomenon where the fraction of damage increases to a threshold value and then stabilizes. This is observed both during single discharging processes and in multiple cycle simulations. In the multi-

cycle analysis, the charging process following the initial discharging leads to a "re-saturation" where the fracture experiences a second increase and then stops growing ever after.

The impedance study suggests that the generation of fracture leads to increase in impedance response of electrode particles. The calculated impedance results are found to be directly related to current density and particle size but drops with increasing temperatures.

DEDICATION

To my parents, Grandpa Qingming, Grandpa Fan, and Chong Wang

ACKNOWLEDGEMENTS

I would like to thank my committee chair, Dr. Mukherjee, for his instruction and encouragement all over the course of this work. This journey would not have been so enjoyable or even possible without his guidance and support. He is not only an academic mentor but also a life-time role model.

I also thank my committee members, Dr. Banerjee and Dr. Efendiev, for their valuable advice and for their careful review of this thesis.

Thanks also go to my brilliant lab partner and friend Pallab Barai, whose suggestions and help are the key to the completion of this work. The support and help from my other lab partner, Seongkoo Cho, are also greatly appreciated. I am so blessed to have worked with you guys.

Finally, I would like to hereby extend my gratitude to Zhixiao Liu, Mohammed Hassan, all ETSL teammates, and to everyone that has come into my life during the last two years and made it better, especially Gary D. Bradley, Stephanie Coleman, the Coleman family, Travis and Michelle Cable, and Alain Anderson.

NOMENCLATURE

A Effective cell surface area for heat convection [m^2]

A_0 Constant coefficient in electrolyte model

c_s, c_{surf} Bulk concentration, surface concentration of lithium ion [mol/m^3]

C_p Specific heat of electrode material [J/(kg·K)]

d Diffusion expansion coefficient [m^3/mol]

D, D_{ref} Diffusion coefficient, diffusion coefficient at reference temperature [m^2/s]

Ea_d Diffusivity activation energy [KJ/mol]

Ea_r Reaction rate activation energy [KJ/mol]

h Heat transfer coefficient [W/ (m^2·K)]

$i_{0,1}$ Constant exchange current density, [A]

$i_{n,faradaic}$ Faradaic current density [A]

I Current density drawn from the cell [A]

k, k_{ref} Reaction constant, reaction constant at reference temperature [$m^{2.5}/(mol^{0.5}s)$]

k_s Stiffness of spring element in random lattice spring model [N/m]

l Length of spring element in random lattice spring model [m]

r Coordinate variable, distance to the center of the spherical particle [m]

R	Universal gas constant [J/(mol·K)]
R_{cell}	Cell Resistance due to electrolyte [ohm]
R_{ct1}	Resistance term at the solid-electrolyte interface in equivalent circuit model of single electrode particle [ohm]
R_s	Radius of spherical particle [m]
t	Simulation time [s]
T	Cell temperature [K]
T_{amb}, T_{ref}	Ambient temperature, reference temperature [K]
u	Displacement of local spring element in random lattice spring model [m]
U_n, U_p	Open circuit potential of negative electrode, positive electrode [V]
v	Cell volume [m^3]
V_{cell}	Voltage output of the lithium ion cell [V]
$Z_{faradaic}$	Impedance of faradaic reaction [ohm]
Z_D	Diffusion induced impedance component [ohm]
Φ_1, Φ_2	Solid phase potential, solution phase potential [V]
ψ	Energy of the local spring element in random lattice spring model [J]
α_a, α_c	Transfer coefficient at anode, cathode, assuming $\alpha_a + \alpha_c = 1$
η_n, η_p	Overpotential at negative electrode, positive electrode [V]
ρ	Density of electrode material [kg/m^3]

ω Frequency of the applied signal in EIS measurement [Hz]

TABLE OF CONTENTS

LIST OF FIGURES

x

LIST OF TABLES

CHAPTER I

INTRODUCTION AND LITERATURE REVIEW

Energy crisis and global warming have become two severe issues facing the human race. It is widely concluded that vehicles driven by conventional engines contribute significantly to energy consumption, air pollution and climate change. In light of this, developing non-fossil fuels for cars would constitute one of most direct approach to resolving these concerns. Electric vehicles powered by battery packs are more efficient and environment friendly that those with internal combustion engines. However, electric vehicles face tremendous battery-related challenges such as charging time, drive range and safety issues. As a high-energy-density secondary source, lithium-ion batteries (LIBs) are currently among the leading candidates for hybrid-and pure electric-vehicle power sources [1, 2]. In order to achieve a better performance, durability and safety, a thorough understanding of lithium ion battery is imperative.

LIBs operate on a rocking chair principle [3]. A typical lithium-ion cell consists of a graphite anode and a $LiCoO_2$ cathode on either side of a porous separator. The schematic shown in Figure 1 illustrates the cell configuration and basic operating principles. The separator only allows lithium-ions to travel through and thus force the electrons into the external circuit. It is during the process of electrons flowing through external circuit that useful work is extracted. Lithium ions, which can be inserted into or extracted from graphite and $LiCoO_2$, travel from anode to the cathode when discharging and back during charge. The commuting of lithium ions between the two electrodes is

1

vividly described as "Rocking Chair". It is this reversible lithium-ion intercalation from both electrodes that makes LIB a rechargeable energy source.
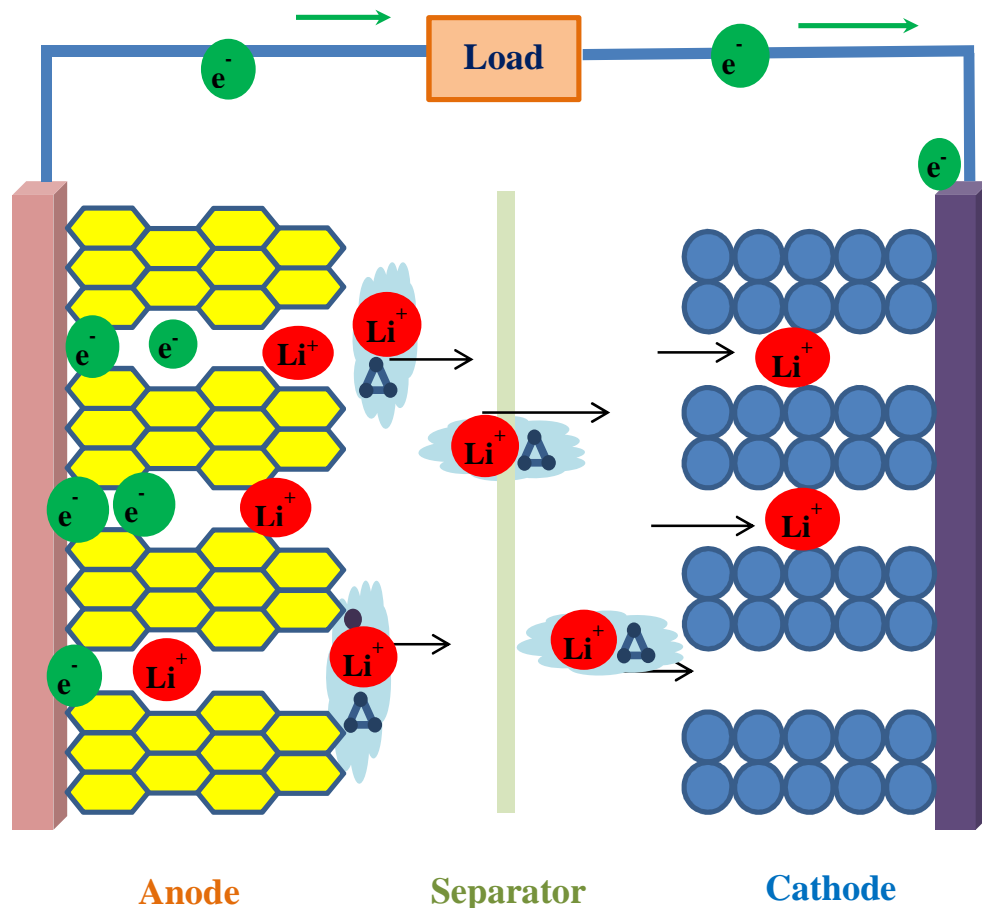

Figure 1 Schematic of structure and operating principle of Lithium-Ion Battery

The insertion and de-insertion of lithium ions stem from two half reactions on positive and negative electrode, respectively:

$$LiCoO_2 \rightleftharpoons CoO_2 + Li^+ + e^-$$ (1)

$$C + Li^+ + e^- \rightleftharpoons LiC$$ (2)

Despite the many and varied types, the two half reactions for an electrochemical cell are very similar. The unique property of Li is that, in such reactions, it releases the most energy albeit the least molecular mass. This endows the lithium-ion battery a unique advantage that cells made with other known materials would never possibly exceed: highest energy density. In figure 1, the lithium ions are released from the graphite electrode side and heading to the metal electrode, indicating that this is a discharging process. As stated earlier, a reverse trip for the lithium ions will be taken in a charging process. During first few cycles, some electrolyte molecule traveling along with lithium ion may react with electrons on the of surface of graphite electrode or $LiCoO_2$ electrode, depending on the direction of current through the cell, and thus form an interface film between the solid phase of electrode and the solution phase of electrolyte [4]. It is called solid electrolyte interface (SEI) film. The existence of this thin SEI film gives rise to both desirable and undesirable changes in battery operations, as will be discussed later in this work.

It is now necessary to clarify the definition of anode and cathode for this work. An electrochemical cell has two electrodes: anode and cathode. The anode refers to the electrode at which electrons get out of the cell and oxidation occurs, and the cathode the electrode at which electrons move into the cell and reduction occurs. In a secondary battery, each electrode may become either the anode or the cathode depending on it is charging or discharging that is ongoing. In order to avoid confusions, this work, unless indicated otherwise, will name graphite electrode anode or negative electrode, and metal electrode cathode or positive electrode.

3

In practice, the primary material for anode is graphitized carbon, with silicon as a major alternative [5-6]. On the other hand, layered $LiCoO_2$ is widely used as cathode material and other choices include $LiFePO_4$ and $LiMnPO_4$ [7]. Although other materials may also be discussed, this thesis considers graphitized carbon and $LiCoO_2$ as anode and cathode materials, respectively.

Lithiation   **De-lithiation**
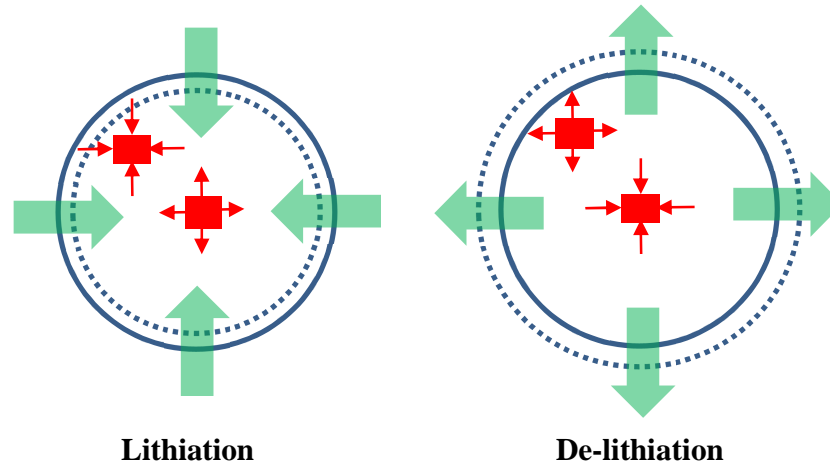
Figure 2 Diagram of lithiation and delithiation induced stress

As a matter of fact, the intercalation and de-intercalation process also pose a threat on LIBs' performance and durability. During lithiation or de-lithiation, the volume of electrode particles experiences a significant change in volume and thus gives rise to considerable internal stress, as illustrated in Figure 2. The resulted stress can then serve as driving force to surface cracks [8-10], as shown in Figure 3. The diffusion induced stress not only creates crack on the electrode particle surface but also enables the existing inside fissure to propagate into surrounding area. The cracks or fractures then act as gaps in the continuum of electrode materials, hindering the transport of lithium

ions in solid phase. As they keep extending and growing, fissures may have a certain area fully enclosed, therefore isolating the lithium ions inside and causing direct performance degradation and permanent capacity loss. The propagation of pre-existing cracks caused by diffusion induced stress could also lead to the growth of SEI on the newly created electrode surfaces. Since lithium is consumed in forming the new SEI, irreversible capacity loss occurs and continues with cycling [11]. It is, then, imperative to understand the mechanical behavior of battery electrodes.
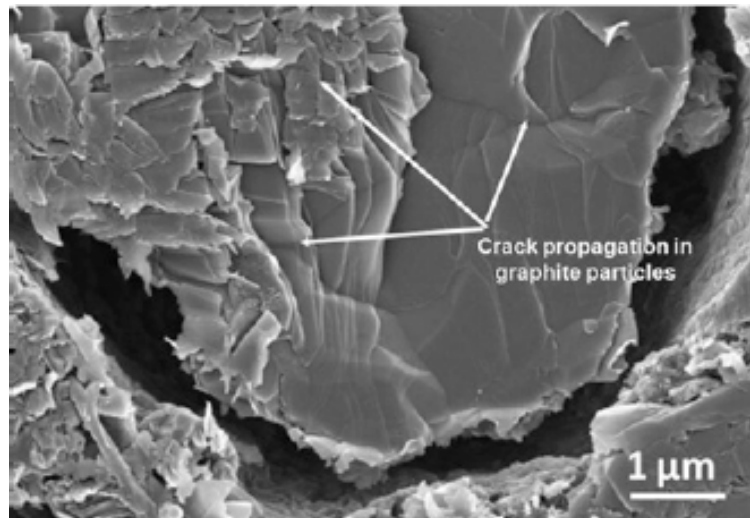
Figure 3 Cracks created by lithiation of a graphite electrode [9]

Meanwhile, temperature has been long known as a factor that greatly affects the performance, safety, and life of LIBs. A schematic of temperature's path to affect the battery can be seen in Figure 4. As an electrochemical system, LIBs rely on half reactions on anode and cathode, both closely related to temperature. The temperature's effect on electrochemical side is fairly clear. It determines the rate and extent to which

5

chemical reactions can occur. Electrochemical reactions can lose their kinetics at low temperatures and can go out of control at high temperatures [12]. This consists of the root cause of a limited temperature range for LIB operation. Even in an ordinary temperature range, the performances of LIBs are very sensitive to operating temperature or ambient temperature.

Temperature's influence on mechanical behavior, however, is yet to be investigated. In reality, different factors interact with each other in the complex operating mechanism of li ion battery. The importance of combining the thermal and mechanical behavior in one comprehensive study presents itself as industry calls for LIBs with even higher and performance and greater durability.

Figure 4 Diagram of temperature effect on power, capacity and life of LIB

Literature Review

The intercalation and de-intercalation induces stress to electrode particle and changes Li-ion transport mechanism [13-15]. Christian and Newman developed a mathematic model to estimate the volume change and the stress induced by the intercalation and de-intercalation process [14]. The model predicts increasing stress with increasing particle size o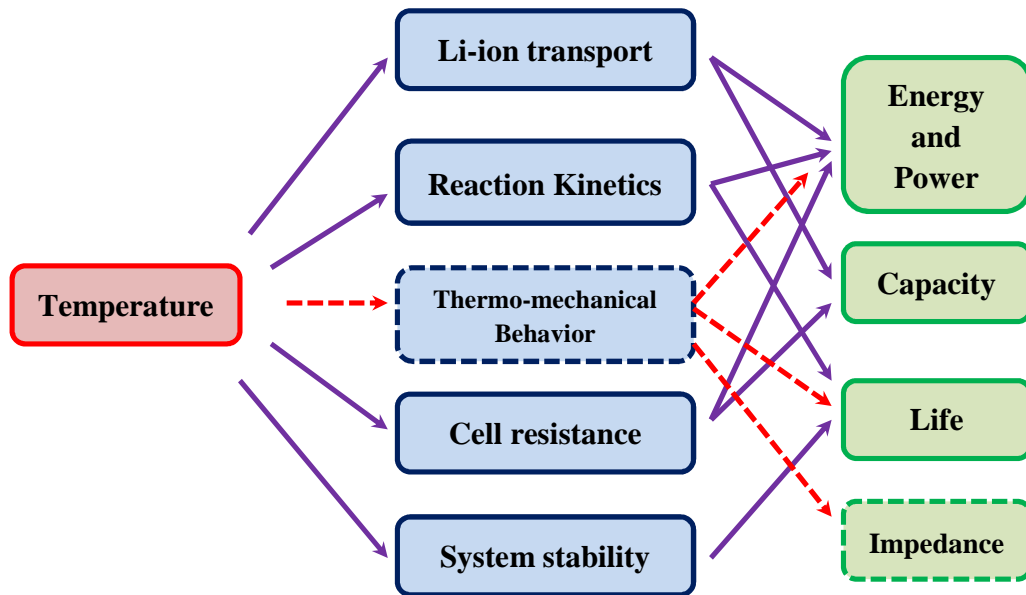r increasing charging or discharging rate and decreasing stress with increasing diffusion coefficient. The authors extend the above mode to investigate the stress generation and fracture in Lithium Manganese Oxide [15].

Smaller particle size was recommended for high C-rate applications to avoid severe fracture generation. A fracture mechanics failure criterion derived by W. H. Woodford predicts for electrode particles a critical current density above which the fracture will be generated. This critical C-rate decreases with increasing particle size, meaning that larger particle tend to experience fracture damage [16]. Kalnanus et al. evaluate the intercalation stress by using a diffusion and elasticity equation with relevant volumetric expansion terms [17]. Their work predicts a critical particle size below which the fracture during lithiation is suppressed.

Zhu at al. adopt an extended finite element method to analyze the propagation of initial crack in ellipsoidal cathode particles under different current density, particle size and particle aspect ratios [18]. As can be expected, the fracture propagation is found to be positively correlated to both current density and particle size. 1.5:1 was identified as the worst aspect ratio in terms of that it requires the lowest current density for the initial

7

crack to grow. Another analysis on the intercalation induced stress in cathode particles was conducted by Zhang et al., where the authors confirmed in spherical particles larger particle sizes and larger discharge current densities give larger intercalation-induced stresses [19]. More interestingly, large aspect ratios are reported to have reduced the intercalation-induced stresses. Later, these researchers take into account not only the particle shape but the heat generation as well [20]. The proposed model considers resistive heating, heat of mixing and entropic heat as three major heat generation sources.

A recent model for a pouch type of Li polymer battery developed by Fu et al. includes electrochemical, thermal and mechanical principles [21]. One interesting conclusion of this work is that, at high C-rate, maximum stress happens at the beginning of charging or discharging process. Gao and Zhou conclude in their analysis of coupled mechano-diffusional driving forces that high lithium concentration moderates the crack growth in Li/Si electrodes [22].

A comprehensive review of thermal issues in lithium ion batteries is presented by Bandhauer at al. [23]. Many researchers have gone great lengths to develop models of thermal behavior of lithium ion batteries. Early in 1990s, Newman and Tidemann solved the basic heat conduction equation in solid phase to calculate the temperature rise in a battery module [24]. With the super power of today's computer technology, the techniques employed by the authors then, such as nondimentionalizaion or superposition, are no longer necessary now. By adopting a volume-averaging technique, Gu and Wang derived a thermal energy equation based on first principles [25]. The fully

8

coupled model was used to simulate the thermal and electrochemical behaviors of a Ni-MH battery, and the temperature was found to have made a significant difference. This model was then extended for Li ion cells by Srinivasan and Wang [26], where it integrates reversible heat, irreversible heat and ohmic heats with temperature-dependent kinetic parameters. Finite element method is also employed to evaluate the thermal behavior in Li ion cells [27, 28]. Guo et al. coupled the thermal effect into a single-particle model of a Li ion cell [29]. Simulation results provided in this work show the temperature rise in a li-ion cell increases with decreasing ambient temperature. Ji et al. analyze the Li ion cell performance in cold temperatures and detail the heat sources that determine the temperature evolution inside the cell [30]. An interesting voltage rebound at low temperatures was observed by the authors. Barai and Mukherjee developed a stochastic methodology to predict the diffusion induced damage in electrode particles and laid the foundation of the hereby presented study [31]. A single particle model with random spring elements and solid phase diffusion was established to simulate the fracture generation inside battery electrodes. This study laid the foundation of the presented work and will be detailed in later chapters.

Electrochemical impedance spectroscopy (EIS) is an ex-stu technique that measures the response of an electrochemical system to a small perturbing current or voltage. Meyers et al. developed a mathematic model to predict the impedance response of a single electrode particle with solid electrolyte interface effect [32]. The model captured fundamental properties of the charger-transfer, double layer and Lithium-ion diffusion in solid phase. A later work by Levi and Aurbach proposed a

nonhomogeneous, layered distribution model of electrode's active mass and finite values of solid phase conductivity [33]. The authors also compare the effect on diffusion of the geometry of spherical and slab particles. Huang et al. assumes two distinct homogeneous phases in the particle due to the insertion and extraction of Lithium ions [34]. This model was used to explore the effect of the state of charge, Lithium diffusivity, SEI, and particle distribution on the total impedance of a LIB. The modeling of inter-particle transport in porous electrodes can be found in the semi-mathematical model developed by Sunde et al [35]. As a common approach to characterize li ion batteries, EIS is also used to evaluate the influence of operating temperature on the performance of LIB. The measured dynamic response covers a frequency range from 10^{-6}Hz to 10^{6}MHz, and the typical frequencies largely depend on the design parameter and manufacturing process [36]. A strong nonlinear temperature correlation was experimentally revealed by D. Andre et al. for all frequency domains [37]. The authors believe the SEI resistance and double layer resistance experience a strong increase at low temperatures where the ions have a lower kinetic energy and move slower.

Summary

The main objective of this work is to identify the thermo-mechanical behavior of LIB electrode particles. As a follow up of the previous research by Barai and Mukherjee [31], the current work will include the thermal effect into the existing single particle model and combine it with impedance computations. It focuses on two parts: fracture generation as well as cell performance with active thermal effect and impedance response under different temperature and fracture scenarios. Particular attention will be

10

paid to the anode electrode. It is of great interest of this work to investigate the temperature effect on fracture generation in electrode particle and the effect of fracture on EIS impedance response of electrode particles.

CHAPTER II

TEMPERATURE DEPENDENT FRACTURE ANALYSIS

Heat generation in Lithium Ion Batteries (LIBs) during operation has the potential to significantly impact the overall performance. Both the anode and cathode in a Li-ion cell consist of very complex composite microstructures. There exist active materials (graphite particles in anode and LiCoO2 particles in cathode) which are responsible for hosting Li ions. The conductive additives (mostly carbon-black) contribute in increasing the electronic conductivity of the electrode. The binders hold all these active particles and the conductive additives together and give the system mechanical stability. The fourth component is the electrolyte which fills up the voids within the material. During charge and discharge, Li ions flow through the electrolyte and intercalate within the active particles. This entire ion and charge transfer by diffusion process causes heat generation within the electrode. For characterizing the performance of the battery correctly, it is very important to capture the heat generation within the Li-ion cell under operational conditions. A single particle model which can capture the heat generating and temperature evolution within the electrode has been adopted from Guo et al. [29]. In this single particle model several approximations are made: (i) The electrode is assumed as a spherical particle with some effective diffusivity of Li ions. (ii) Lithium ion concentration within the electrolyte is assumed to be constant throughout the electrode. (iii) Uniform intercalation of Lithium ions are assumed from all the directions of the electrode particle. (iv) Lithium ion flux is assumed to be same as

the externally applied current. (v) Voltage of the cell is evaluated as a point function using the average surface concentration of the spherical particle. In the following, the technique adopted to capture the temperature evolution within the electrode particle will be explained.

In a previous work, Barai and Mukherjee developed a stochastic methodology to predict the diffusion induced damage in electrode particles [31]. A circular cross section of the single particle has been taken into consideration to model the diffusion induced stress and capture the fracture observed during operation. The circular cross section of single particle was modeled using random lattice spring formalism. Lithium diffusion in solid state was simulated by solving the Laplace equation with proper boundary conditions using finite volume approach. Temperature evolution and damage inside the electrode, in terms of the fraction of broken bonds, was investigated under different parameters, such as current density, particle size and initial crack locations.

Single Particle Model

A systematic introduction of modeling and simulation of battery system is given by Mukherjee [38]. In a single particle model, each electrode is simplified as a single spherical particle and the potential and Li ions concentration in electrolyte phase are not solved. In a discharging process, for example, the li ions migrate to the surface of negative electrode particle, travel through the electrolyte phase with an assumed infinite diffusivity, reach and enter the positive electrode particle. The electrons, meanwhile, go through the external circuit, render the useful work and finally arrive at the negative electrode as well.
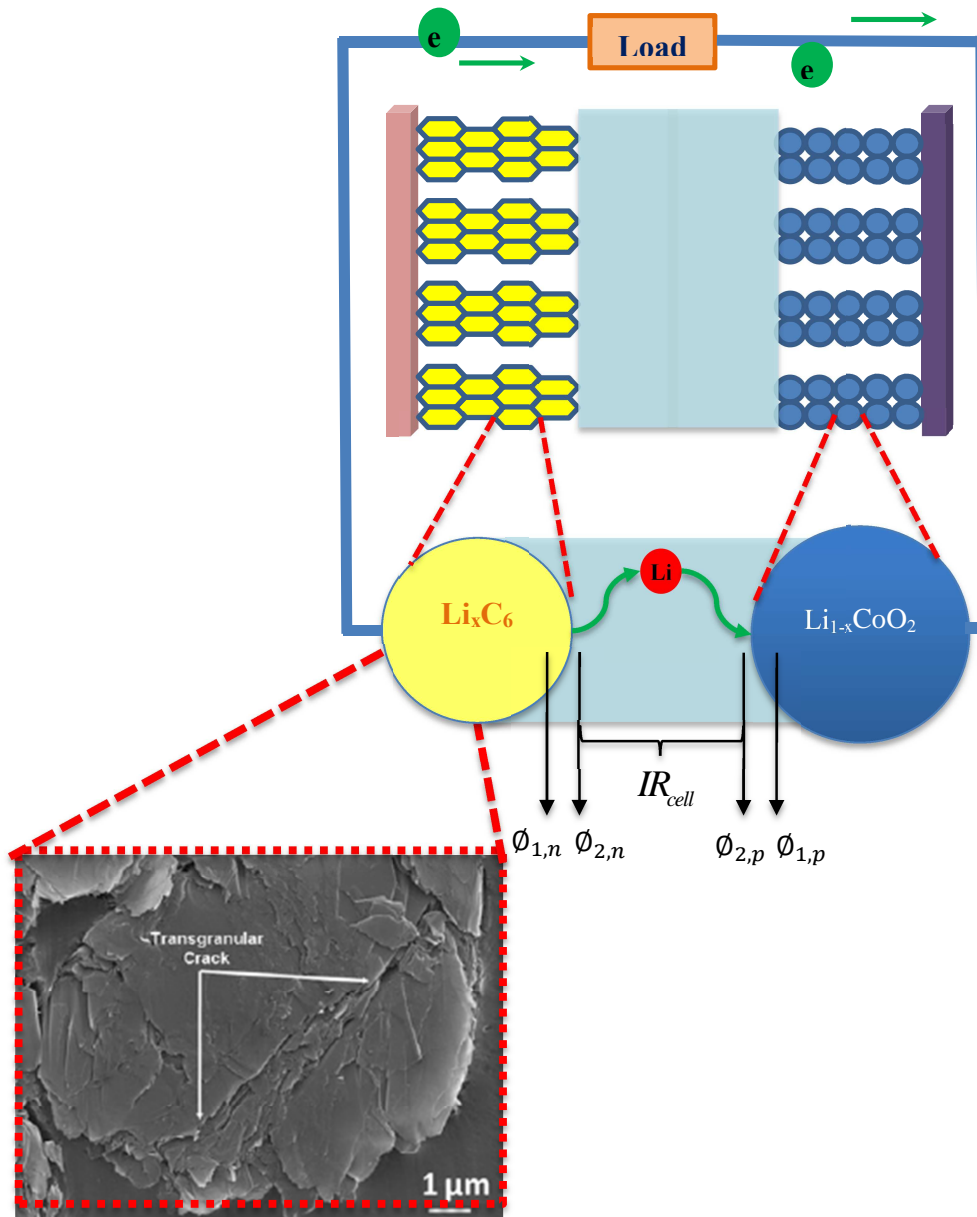
13

Figure 5 A schematic of single particle model of LIB: SEM image source [9]

Figure 5 provides an illustration of which area in an actual graphite particle the author is trying to model and study in this research. The Li-ion concentration profile is obtained by solving

$$\frac{\partial c(\vec{x},t)}{\partial t} = \vec{\nabla} \cdot (D(\vec{x},t) \cdot \vec{\nabla} c(\vec{x},t)) \tag{3}$$

The above governing equation is subject to a boundary condition described as

$$-k_{cond} \frac{\partial c(\vec{x},t)}{\partial n} = \frac{i}{F} \tag{4}$$

In order to consider the mechanical behavior of electrode particle, Barai and Mukherjee developed a stochastic methodology based on a random lattice spring model [31]. In this analysis, the single particle is considered as a circular domain where the entire mass of the particle is assumed to be lumped at each node. Each lumped-mass node connects with six neighbors with lattice spring bonds, as shown in Figure 6. Note the spring elements have stiffness in both axial and transverse directions.
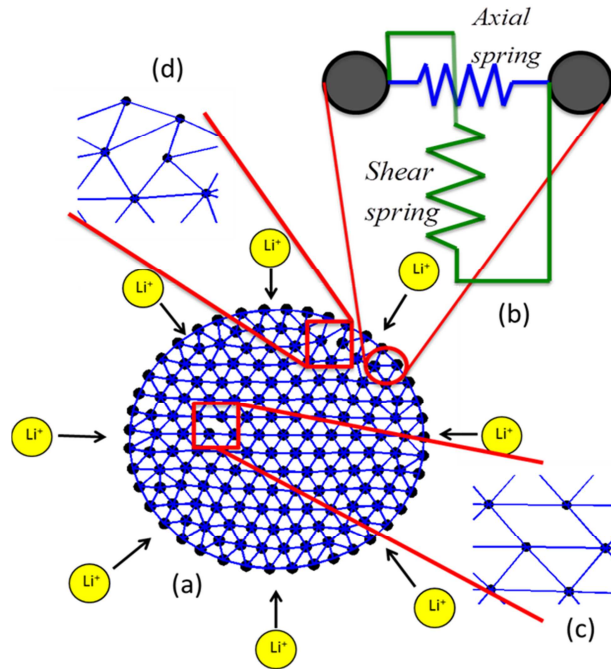

Figure 6 Diagram of random lattice spring single particle model [31]

15

For each spring, the local force is a function of local displacements and can be described as

$$\begin{bmatrix} f_{x1} \\ f_{x2} \\ f_{x3} \\ f_{x4} \end{bmatrix} = \begin{bmatrix} k_n & 0 & -k_n & 0 \\ 0 & k_s & 0 & -k_s \\ -k_n & 0 & k_n & 0 \\ 0 & -k_s & 0 & k_s \end{bmatrix} \begin{bmatrix} u_{x1} \\ u_{x2} \\ u_{x3} \\ u_{x4} \end{bmatrix} \qquad (5)$$

where $\overline{f}$ represents the local force vector and $\overline{u}$ the local displacement vector, k_n is the spring stiffness in axial direction and k_s in the transverse direction. Stress induced by Li ion diffusion is characterized by the resulting axial displacement inside the spring element Δu^d, which is expressed as

$$\Delta u^d = d \cdot \Delta c \cdot l \qquad (6)$$

where d is the diffusion expansion coefficient, Δc the incremental change in Li ion concentration, and l the length of spring element. The global force vector due to diffusion-induced stress, $\overline{F^d}$, is then defined as a function of displacement

$$\overline{F^d} = [T]^T \overline{f^d} = [T]^T [k] \Delta u^d \qquad (7)$$

where $[T]$ is a transformation matrix and $[k]$ the stiffness matrix.

The fracture criterion is related to the total elastic energy stored within a spherical particle due to diffusion-induced stresses [39]. In this work, the generation of fracture or crack is modeled by the breaking down of the spring elements, or in other words, the bonds between nodes. This is realized by a prescribed energy threshold. The energy of each spring element is calculated as

16

$$\psi = \frac{1}{2}\overline{F_{spring}} \cdot \overline{u_{spring}} \tag{8}$$

where $\overline{F_{spring}}$ and $\overline{u_{spring}}$ are the global force and displacement vectors in the related spring element. If the calculated energy exceeds a threshold value, this spring element will be considered broken and removed from the stiffness matrix for further simulation. The threshold value for graphite is identified as $2J/m^2$ [40, 41].

The overpotential η_j ($j = p, n$) is defined as

$$\eta_j = \phi_{1,j} - \phi_{2,j} - U_j \tag{9}$$

where $\phi_{1,j}$ is the solid phase potential, $\phi_{2,j}$ the solution phase potential and U_j the open circuit potential. As shown in Figure 5, this work simplifies the potential drop in the electrolyte as if it were a nonlinear resistor. This gives

$$\phi_{2,p} - \phi_{2,n} = IR_{cell} \tag{10}$$

The cell voltage is then calculated by Eq. (11) and the overpotentials on both electrode are solved from Eq.(12).

$$V_{cell} = U_p - U_n + (\eta_p - \eta_n) + IR_{cell} \tag{11}$$

$$J_j = k_j c_{s,j,\max} c_e^{0.5} \left(1 - x_{j,surf}\right)^{0.5} x_{j,surf}^{0.5} \left[\exp\left(\frac{0.5F}{RT}\eta_j\right) - \exp\left(-\frac{0.5F}{RT}\eta_j\right) \right] \quad (j = p, n) \tag{12}$$

Coupling Thermal Effect

As a follow up, the present work incorporates the thermal effect into previous single particle model by including the following lumped thermal conduction equation

$$\rho v C_p \frac{dT}{dt} = IT \left[\frac{\partial U_p}{\partial T} - \frac{\partial U_n}{\partial T} \right] + I\left(\eta_p - \eta_n + IR_{cell}\right) - hA\left(T - T_{amb}\right) \tag{13}$$

17

In addition, the temperature-dependent parameters, as shown in Figure 7, are upgraded to be a function of temperature. The solid phase diffusion coefficients, reaction rate constant, and the cell resistance, which is inversely proportional to the electrolyte conductivity, all follow an Arrhenius relationship with cell temperature, as expressed in Eq. (14-16).
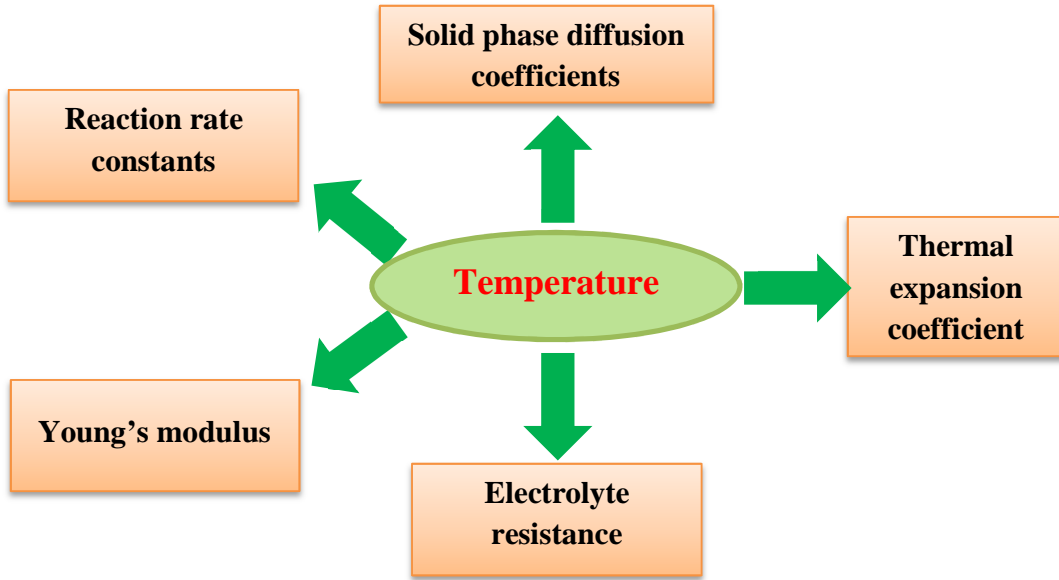

Figure 7 Temperature dependent parameters in the electrochemical system

$$D_j = D_{j,\,ref} \exp\left[\frac{Ea_d}{R}\left(\frac{1}{T_{ref}} - \frac{1}{T} \right) \right] \quad (j = n,\ p) \tag{14}$$

$$k_j = k_{j,\,ref} \exp\left[\frac{Ea_r}{R}\left(\frac{1}{T_{ref}} - \frac{1}{T} \right) \right] \quad (j = n,\ p) \tag{15}$$

$$R_{cell} = R_{ref} \exp\left[A_0 \left(\frac{1}{T} - \frac{1}{T_{ref}} \right) \right]$$ (16)

Theoretically, when an ion transport process involves intermolecular ion hopping, the conductivity will be determined by the thermal hopping frequency that is proportional to the term $e^{-\frac{E}{kT}}$ [42]. This is assumed to be the case over the entire temperature range of interest in this work, which is -20°C to 40°C. Based on this assumption, an expression of electrolyte resistance, in this case, the cell resistance, can be derived as Eq. (16).
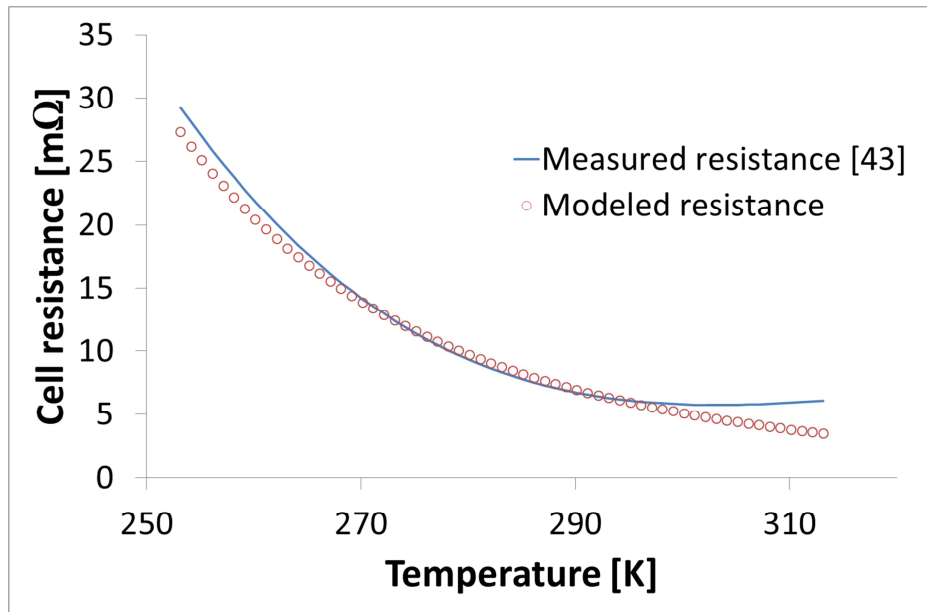

Figure 8 Verification of constant coefficient in resistance model

Note that in order to apply this model, two parameters are required to be known. One is a reference resistance R_{ref} value under a certain temperature T_{ref}. The other is a

constant coefficient A_0, which needs to be determined by a second resistance value measured at another temperature. The value of A_0 characterizes how the electrolyte conductivity or resistance varies with ambient temperatures. In this work, this coefficient was adjusted to match the measured resistance data of a li ion cell used in electric vehicles. As can be seen in Figure 8, the modeled resistance by Eq. (16) agrees with the curve fitted by experimental measurements [43].

The different type of materials are differentiated by Eq. (17), where k_{mat} is a constant and serves to assess the direction and extent to which the material's modulus varies with concentration, and therefore with temperature. When k_{mat} is positive, it represents a type of material whose modulus increases with c. Likewise, if it is negative, the material has a modulus decreasing with c. Particularly, a constant modulus will be true if it is set to be zero.

$$E = E_0\left(1 + K_{mat}\frac{c}{c_{\max}}\right) \tag{17}$$

The open circuit potential U_p and U_n are considered as a function of SOC and temperature in the following expression

$$U_j\left(x_{j,surf},T\right) = U_j\left(x_j\right) + \frac{\partial U_j}{\partial T}\cdot\left(T - T_{ref}\right) \qquad \left(j = p,n\right) \tag{18}$$

where the derivative terms $\dfrac{\partial U_j}{\partial T}$ are given as a function of SOC [29]

$$\frac{\partial U_p}{\partial T} = \frac{-0.19952 + 0.92837x_p - 1.36455x_p^2 + 0.61154x_p^3}{1 - 5.66148x_p + 11.47636x_p^2 - 9.82431x_p^3 + 3.04876x_p^4} \tag{19}$$

$$\frac{\partial U_n}{\partial T} = \frac{0.00527 + 3.29927x_n - 91.79326x_p^2 + 1004.91101x_n^3 - 5812.27813x_n^4 + 19329.7549x_n^5 - 37147.8947x_n^6 + 38379.18127x_n^7 - 16515.05308x_n^8}{1 - 48.09287x_n + 1017.2348x_p^2 - 10481.80419x_n^3 + 59431.30001x_n^4 - 195881.6488x_n^5 + 374577.3152x_n^6 - 385821.1607x_n^7 + 165705.8597x_n^8} \quad (20)$$

Table 1 lists all the values of parameters in the above equations.

Table 1 Global input parameters in fracture simulation

Parameter	Value	Unit
ρ	1626 [29]	Kg/m^3
v	3.38E-05 [29]	m^3
Cp	750 [29]	$J/(kg \bullet K)$
I	1.656	A
T_{ref}	298.15	K
$D_{ref, n}$	3.9E-14 [44]	m^2/s
$D_{ref, p}$	1.0E-14 [44]	m^2/s
$Ea_{d, n}$	35 [45]	KJ/mol
$Ea_{d, p}$	29 [46]	KJ/mol
$Ea_{r, n}$	20 [47]	KJ/mol
$Ea_{r, p}$	58 [48]	KJ/mol
$k_{ref, n}$	1.76E-11 [49]	$m^2/(mol^{0.5}s)$
$k_{ref, p}$	6.7E-11 [49]	$m^2/(mol^{0.5}s)$
R_{ref}	16	$m\Omega$
R	8.3141	$J/(mol \cdot K)$
E_{ref}	70.5	GPa

Table 1 Continued. Global input parameters in fracture simulations

c_{max}	31833[29]	mol/m^3

Results and Discussion

The heat generation, including reversible heat and irreversible heat, are given in Figure 9. The irreversible heat increases significantly as the ambient temperature gets lower. Apparently, the resistance of Li diffusion in electrolyte and through the electrode particles increases drastically with decreasing temperature. Meanwhile, the kinetic activation energy also gets larger as the ambient temperature drops.
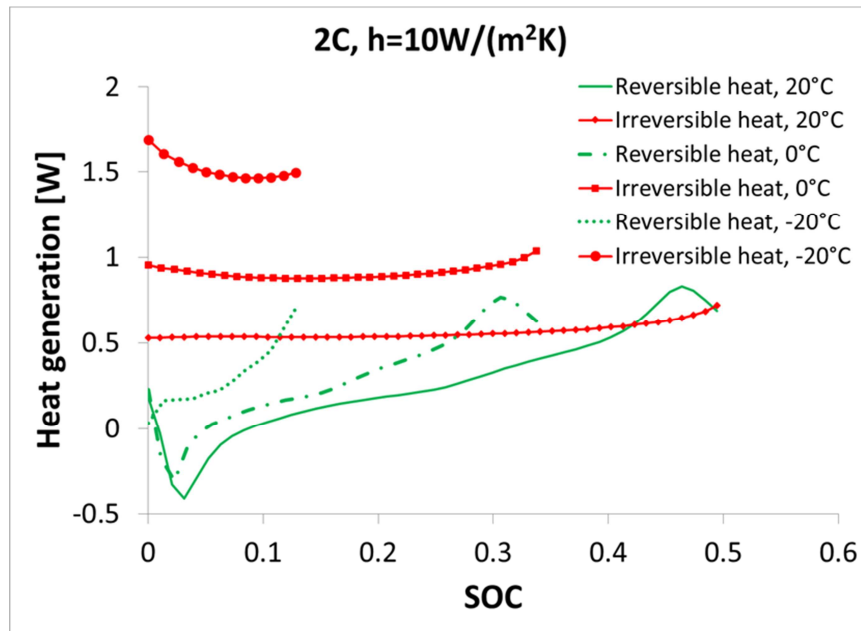

Figure 9 Heat generation at subzero, zero and room temperatures

Note that the reversible heat could be negative at the very beginning of a discharging process, and this may lead to a seemingly odd temperature drop for the cell, when the irreversible heat is not enough to make the total heat generation be positive. Based on what is shown in Figure 9, this mechanism is stronger at room temperature.
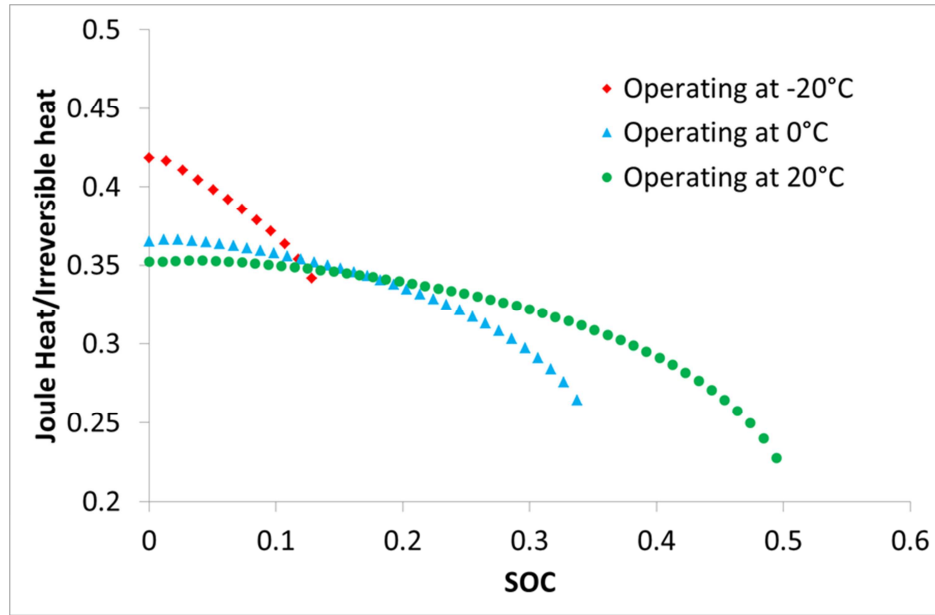

Figure 10 The ratio of joule heat to irreversible heat versus SOC

Figure 10 shows that the proportion of joule heat to irreversible heat decreases in a single discharge process but increases with decreasing ambient temperatures. When discharging, the cell experiences a temperature rise and a consequently resistance drop. On the other hand, the irreversible heat tends to increase as the discharge continues. The ratio between these two thus drops, and this is particularly true at lower temperatures where the cell resistance is even more sensitive to the cell temperature.

23

As discussed above, the heat generation is more significant at subzero temperatures. This explains why the cell displays a larger increase in colder environments, as shown in Figures 11. The same phenomenon were observed and reported by M. Guo et al. [29] and Y. Ji et al. [30]. The current model, by adopting the same parameters and boundary conditions, renders the temperature profiles that greatly match the results reported by M. Guo [29] at all four different temperatures. One explanation for this is that, at low temperatures, the activation energy that needs to overcome for the electrochemical reactions to proceed is significantly larger, resulting to the increase of irreversible heat and consequently a larger temperature rise.
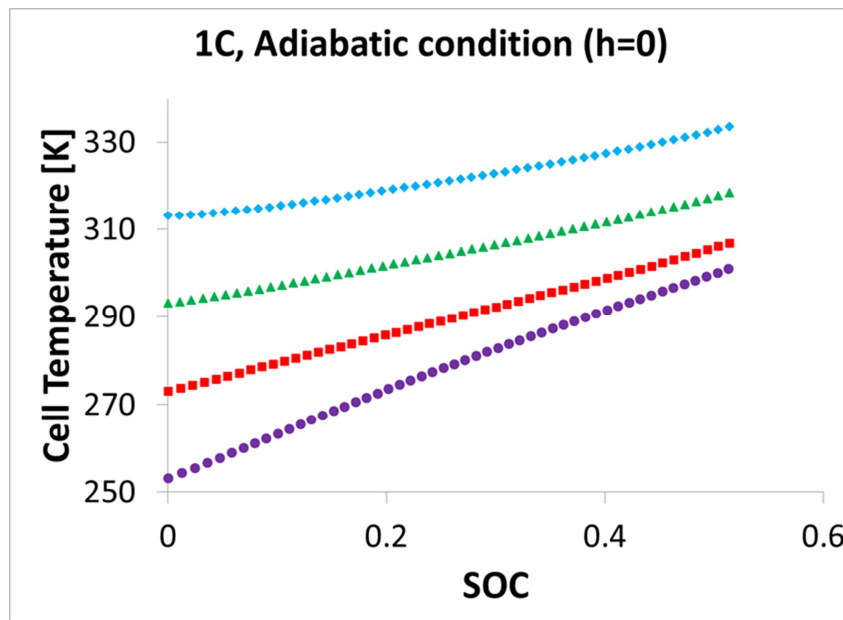

Figure 11 The effect of ambient temperature on cell temperature profile

Cell temperature is also a function of C-rate and heat transfer coefficients, as can be seen in Figures 12 and 13(a). Temperature increase at high C rates can be considerable and may pose a significant threat to the cell performance. A thermal runaway could cause the whole system out of control. The rise in cell temperature is also significant when ambient temperatures are extremely low and heat generation is substantial, except that the temperature rise in this case would be beneficiary and desirable. This is because at low temperatures the ion transport is supposed to be slow but can be boosted by a sudden and huge temperature rise inside the electrode.
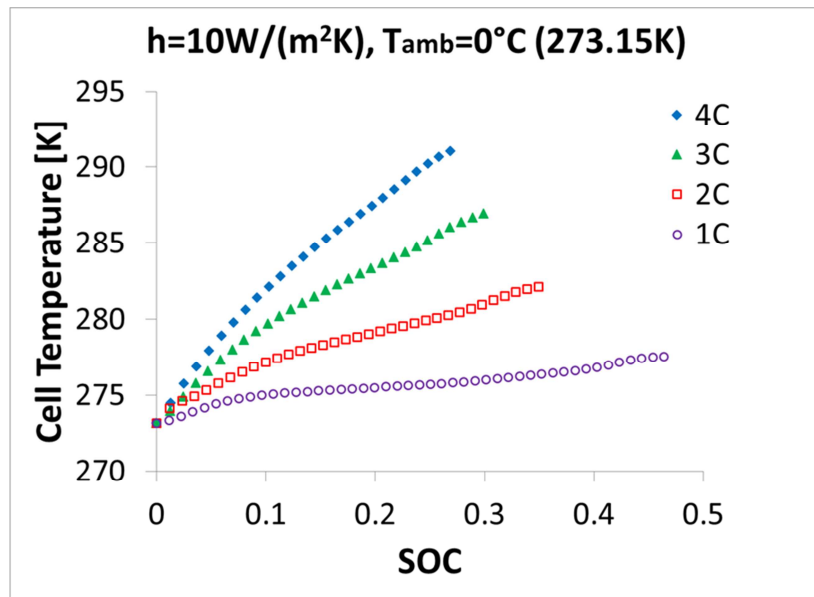

Figure 12 The effect of current density on cell temperature

For vehicles that are to be used in areas with freezing weathers, cold start has been a huge challenge. An effective strategy might be to provide an initial "warming up" or enough insulation to keep the temperature of the engine, in this case, the battery

system above the freezing point. From Figure 13, one can see that the adiabatic condition enables a large temperature rise, and this greatly improves the voltage output from the cell at subzero or zero temperatures.
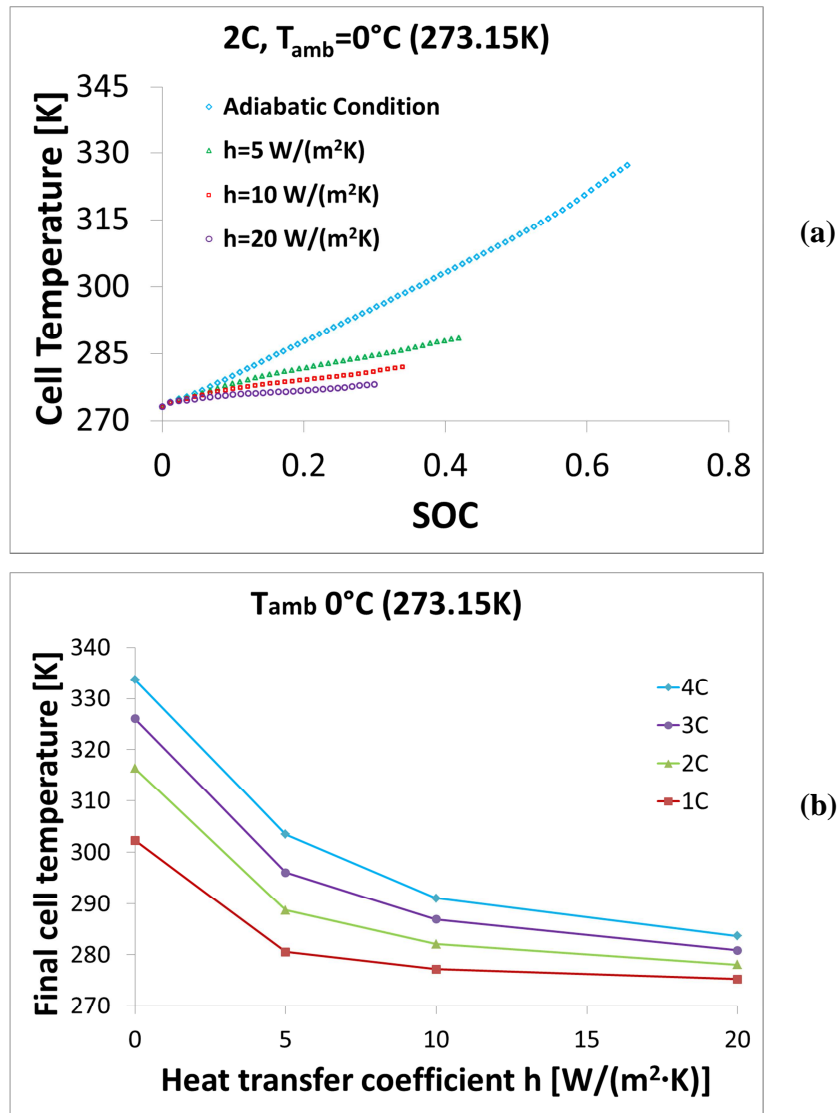

Figure 13 The influence of boundary condition on cell temperature

26

From a design perspective, it is meaningful to define a heat transfer coefficient that suffices the thermal management requirements with minimum cost. In figure 13(b), one can see that cell temperature does drop drastically as h increases from 0 to 5W/(m^{2}K). If doubling h to 10W/(m^{2}K), it also serves to lower the temperature at high C-rates. After that, however, making the heat transfer coefficient larger no longer helps to decrease the cell temperature significantly. For example, if one doubles it again to 20W/(m^{2}K), the resulting temperature decrease is only about 7K.

The temperature rise could boost the cell performance greatly, especially at cold temperatures. Figure 14 shows a voltage rebound, as was observed by Y. Ji [30] in another work, at -20°C with a discharging rate of 1C. Since perfect insulation was assumed, all the heat generated inside the electrode turns to temperature rise. Given the extremely low ambient temperature, the heat generated from the electrochemical reactions is considerable and significantly increases the cell's internal temperature.
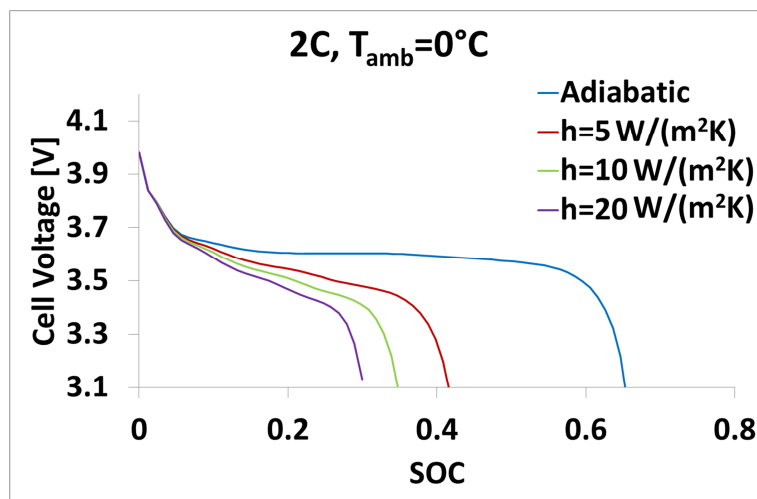

Figure 14 Adiabatic condition leads to voltage rebound at subzero temperatures

This improvement in voltage performance may be associated with the sudden and drastic heat generation warming the diffusivity up. Figure 15 presents a triangle relationship between temperature profile, voltage performance and diffusivity curve. It can be seen that, a huge temperature increase enabled by adiabatic condition lifts the diffusivity to where it is very sensitive to temperature, leading to a considerable enhancement in cell performance. In other cases, the modeled surface concentration of li ions quickly reached zero and the simulated discharging process was then forced to be terminated. The corresponding voltage outputs were poor.
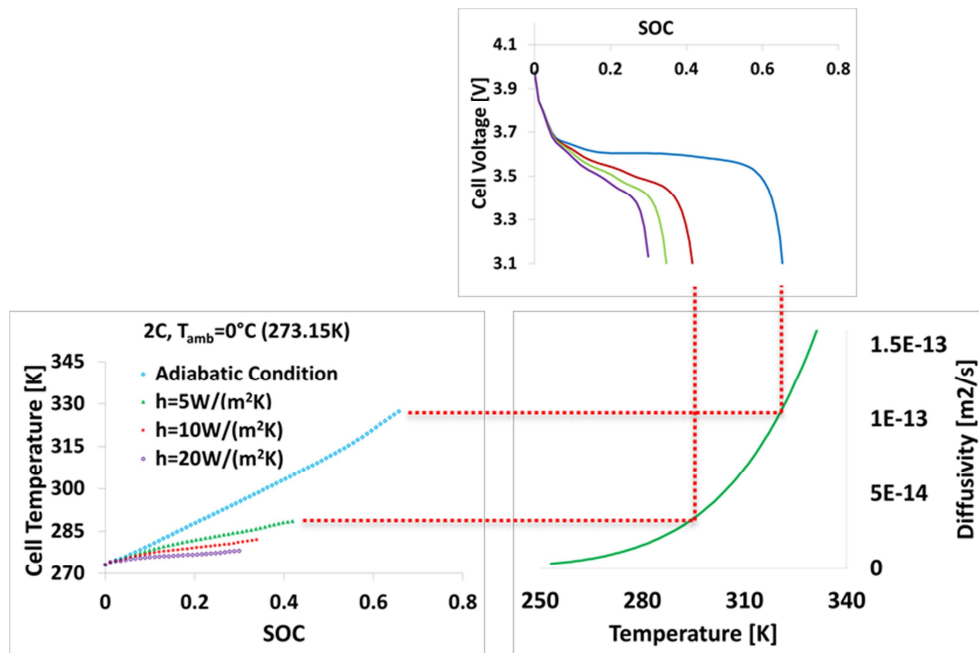

Figure 15 The triangle relationship between cell temperature, diffusivity and voltage output

Figure 16 depicts the fracture and ions concentration profile inside the electrode particle after a discharging process was completed. The fracture damage is seen to be more serious at 4C, the highest current density in the simulation. The higher the current density drawn from a cell, the larger the lithium ion concentration gradient inside the electrode particle. A comparatively larger concentration gradient, as can be expected, leads to stronger lithiation or delithiation stress and consequently more fracture damage inside the particle.
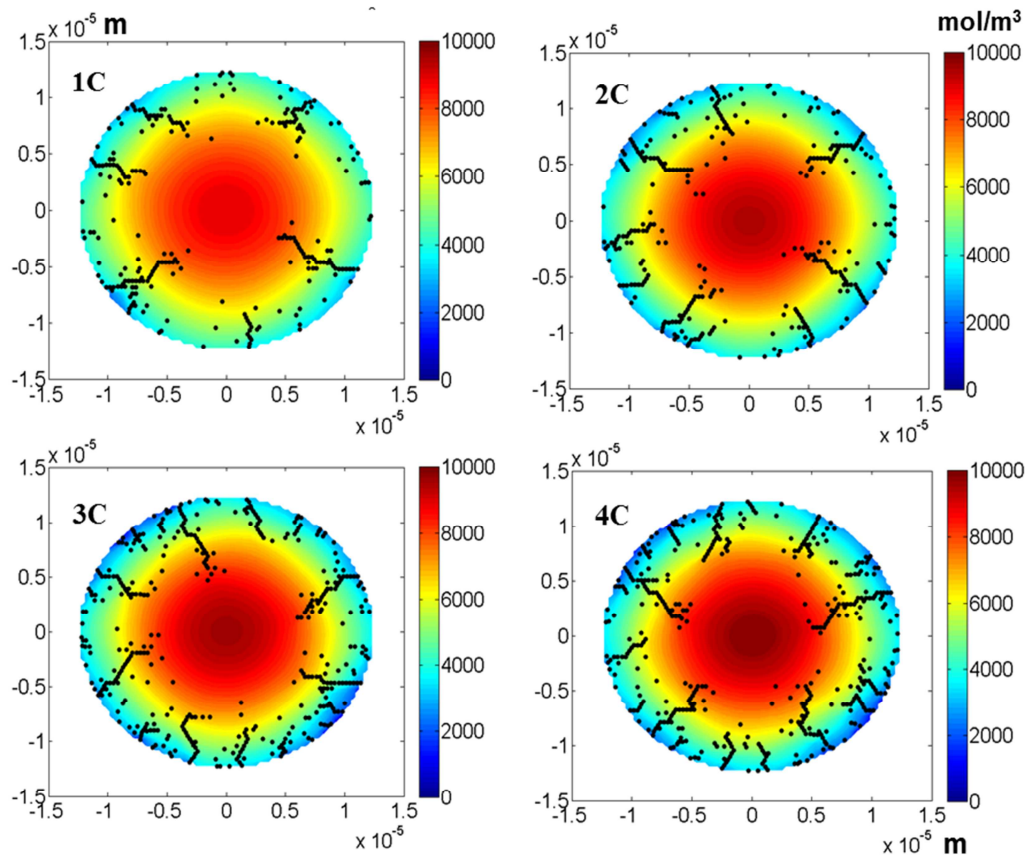

Figure 16 Simulated fracture distribution in an electrode particle, at 273K, adiabatic condition.

The voltage output with and without fracture effect is compared in Figure 17. The existence of fracture, not surprisingly, accelerates the voltage degradation. The formation of fracture blocks the diffusion of lithium ions and results into considerable voltage loss. Generally, the damage induced by the lithiation and delithiation are shown to be positively correlated to the current density, as can be seen from Figure 18. This is proven to be true for all four different simulated temperatures, if an adiabatic condition is considered. When a heat transfer coefficient of 10 $W/(m^2 \bullet K)$ is applied, the trend shown in Figure 18 will slightly change. The damage fracture drops with current density, as the evolution time of fracture becomes shorter than enough for the damage to propogate.
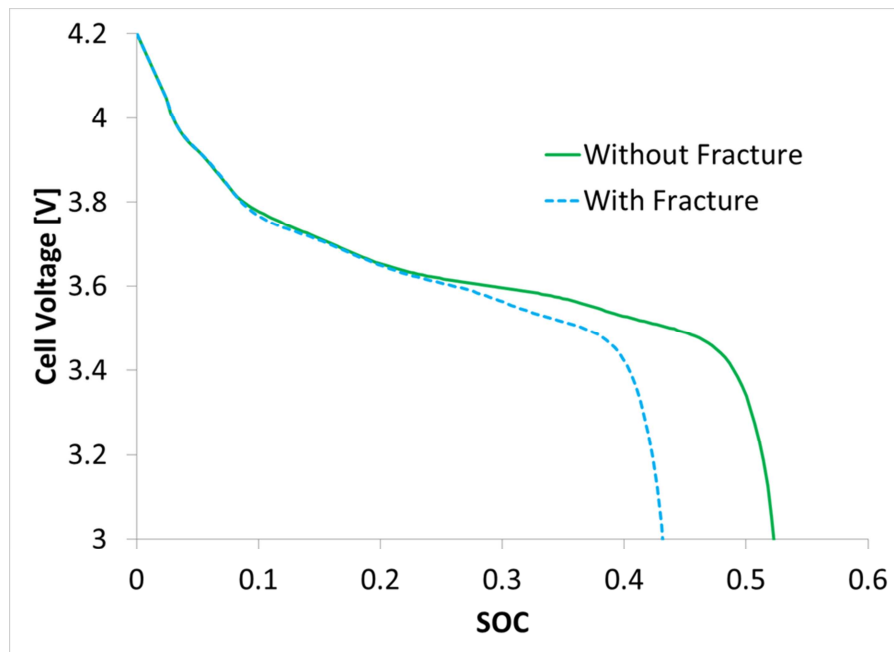

Figure 17 A comparison of the voltage curve: with and without fracture effect at the temperature of 20 ºC, 1C
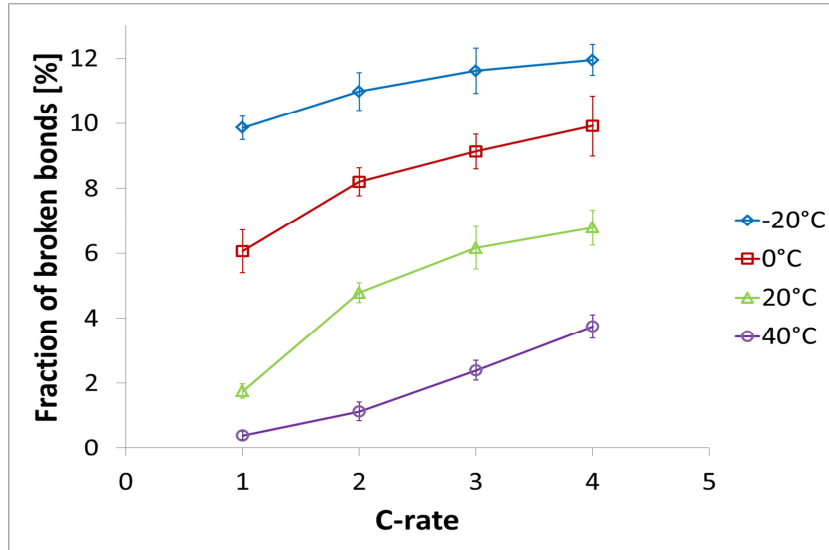
Figure 18 Fraction of broken bonds versus C-rate at four ambient temperatures, adiabatic condition
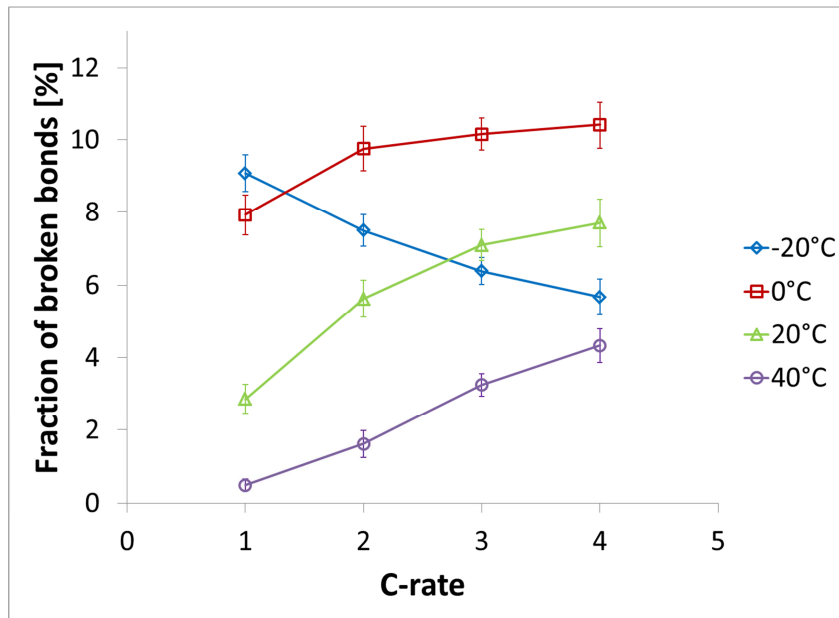

Figure 19 Fraction of broken bonds versus C-rate, h=10 W/(m^2•K)

31

Although it remains to be true that high C-rate leads to larger amount of damage at zero and above-zero temperatures, the fraction of broken bonds drops with increasing current density at -20ºC. The diffusivity of the system is extremely low and lithium ion concentration gradient does not develop completely at such freezing temperatures. The discharging process ends even more quickly at higher C-rate and the fracture damage does not have time to evolve at all, despite the even stronger potential harm.

The temperature rise and the consequently better diffusivity enabled by adiabatic condition render a smaller concentration gradient through the particle and thus tend to alleviate the damage. On the other hand, however, these two factors also give rise to a
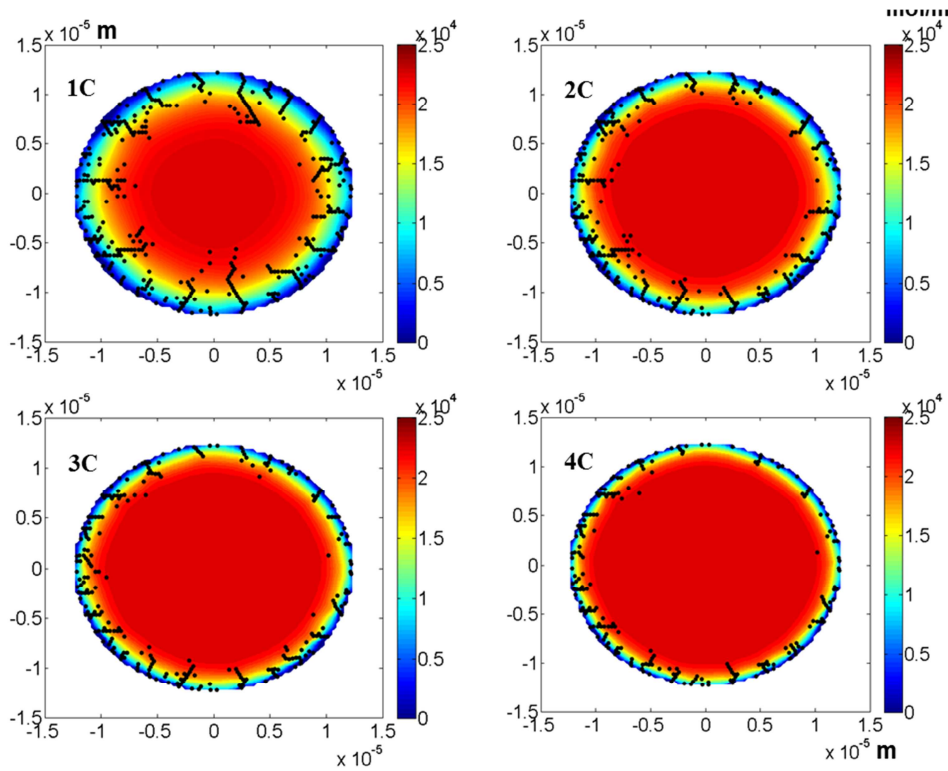

Figure 20 Fracture distribution inside electrode particle, at 253K, h=10 W/(m²•K)

more durable discharging process. The extended time allows fracture damage to evolve and propagate to its vicinity. The later seems to become the dominating mechanism when the cell operates at subzero temperatures. Adiabatic boundary condition leads to larger fraction of broken bonds, as can be found by a comparison between Figure 16 and Figure 20. At a comparatively higher temperature, for instance, 0°C, the former tends to be the governing mechanism and the fracture damage induced by lithiation and de-lithiation is much less, as can be seen in Figure19 and Figure 20. Temperature rise obviously alleviate the fracture damage, probably by improving the diffusivity.
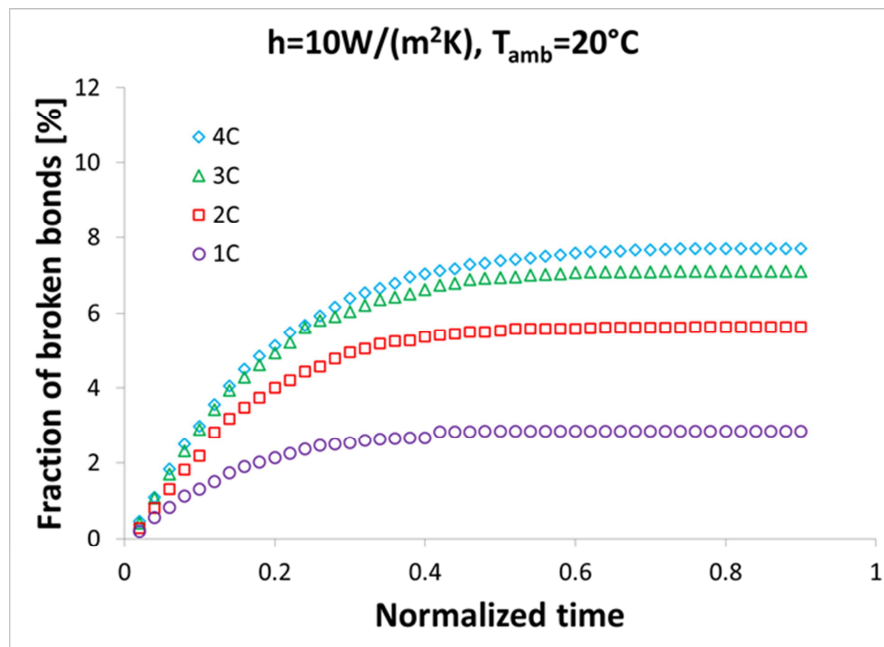

Figure 21 The transit fracture evolution profile with time

Figure 21 shows the transient growing process of fracture inside the electrode particle. As discussed earlier, the fraction of broken bonds increases with decreasing ambient temperature, as long as the initial temperature does not significantly shorten the discharge time. Given enough time to grow, the fracture would reach a steady state, like "saturation". At any particular C-rate, the number of broken bonds stops increasing after exceeding a certain threshold value, which is desirable in terms of that the damage is restricted to a certain limit because of the fact that sufficient amount of strain energy is released by the already existing cracks. Particularly, the number of broken bonds may stop increasing before reaching the saturation point when operating at cold temperatures, as shown in Figure 22.
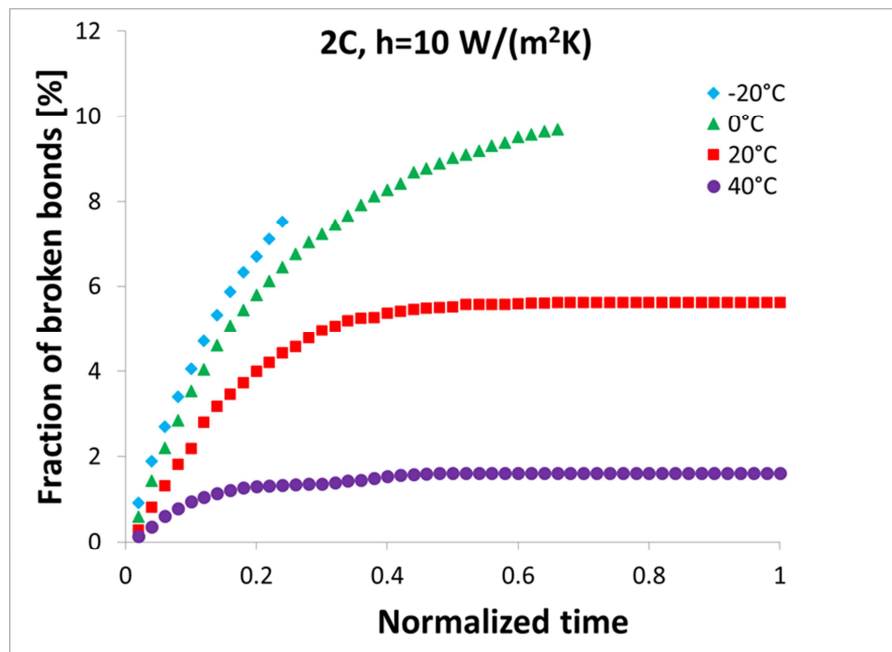

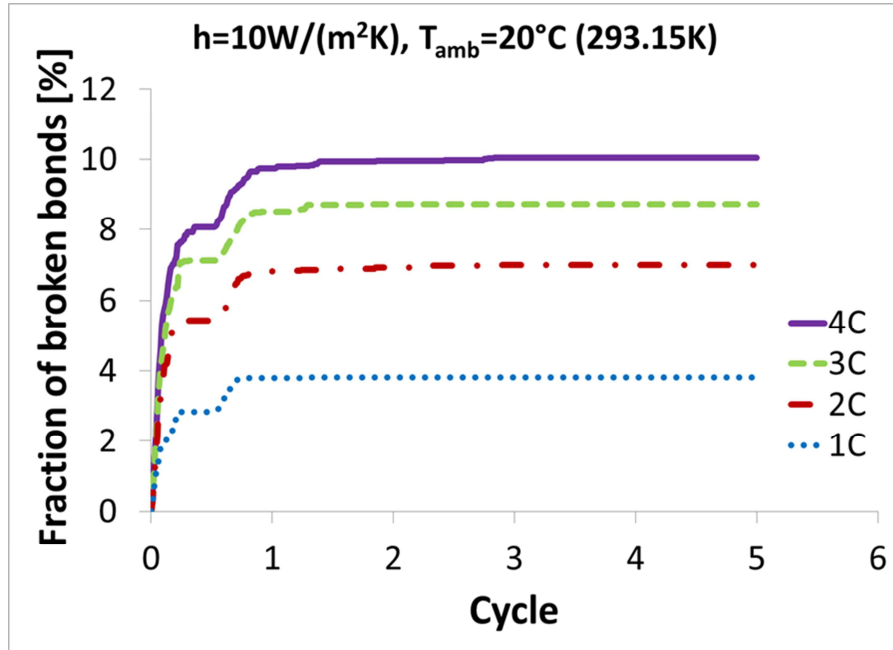**Figure 22 Fracture evoluion profile at lower temperature: 0°C**

Figure 23 Fracture behavior in multi-cycle simulation

The fracture behavior is also investigated from a cycle by cycle perspective. Figure 23 shows that the fracture evolution reaches a steady state after the first cycle, one single entire discharge-charge process. Specifically, the broken bonds increases and reach a saturation status in the first discharge process. The ensuing charging process trigger the fracture evolution again and it re-saturate after a comparatively smaller increase. The damage is mainly caused in the first cycle, although a nearly negligible amount of new broken bonds are observed in the second or third cycles for high C-rates like 4C.

Figure 24 present a positive relationship between particle damage and particle size at room temperature, 20°C. Fracture of broken bonds typically is higher in larger particles and it seems that there will be no fracture generated if the particle size is below

35

a critical size. It has been reported that both the intensity and distribution of stress is quite sensitive to surface mechanics when the particle diameter reduces to the nanometer range [50]. Surface energy and surface stress can serve to alleviate diffusion induced stress in nanostructured electrodes [51]. For example, a tensile state of stress could either drop in magnitude or even be reverted to a state of compressive stress in particles with nanometer-level radius.
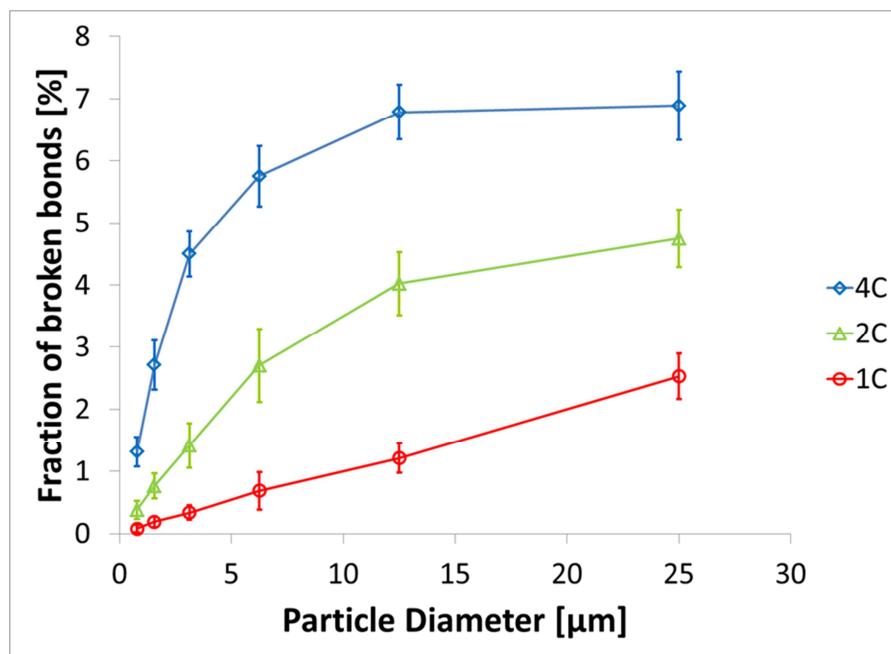

Figure 24 The effect of particle size on fracture damage

In addition, the material property of electrode particles could have a bearing on the diffusion induced damage [52]. The concentration dependent elastic modulus is believed to significantly affect the peak stress and stress evolution in the electrodes [53].

The young's modulus of a material may vary as lithium ion concentration changes during the charging or discharging.
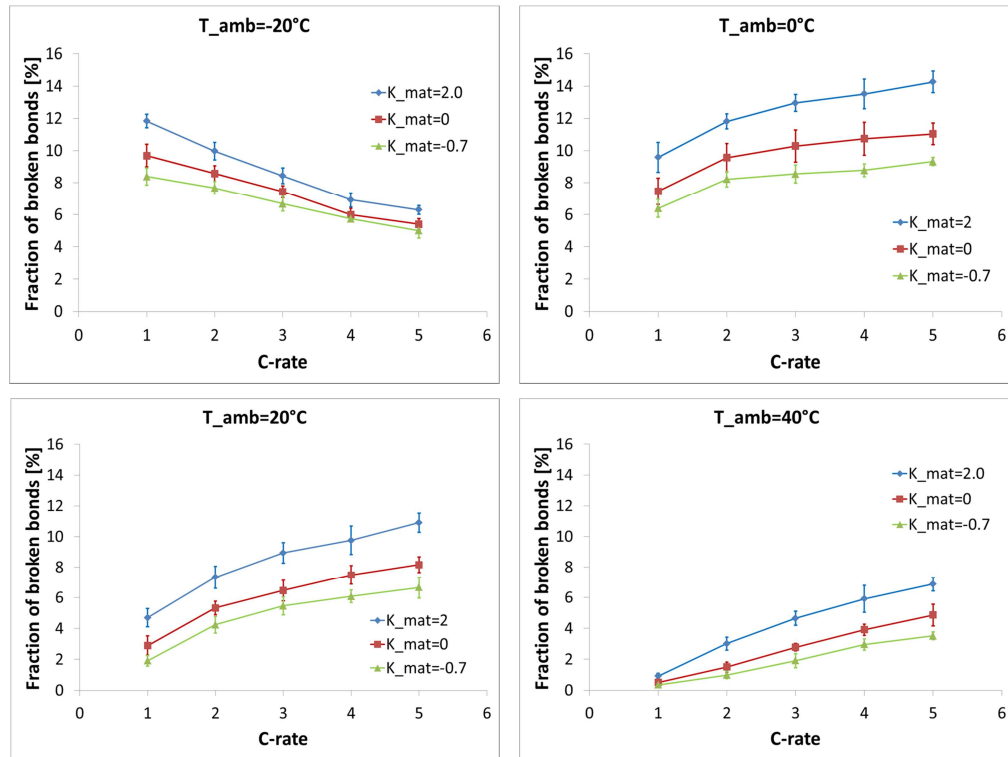
Figure 25 The impact of Young's modulus on fracture formation

Figure 25 shows that, over the entire temperature range of interest, Si type material, represented by a negative value of -0.7, display a better immunity to particle fracture damage. Simulation conducted for graphite type material with a value of 2 predicts 14% damage in graphite type electrode particles. Results calculated using a constant Young's modulus display a medium fraction of broken bonds, as expected. An interesting detail in the results is that the fraction of broken bonds related to Si type

material is the least sensitive to current density in both cold and high temperatures. This suggests that this type of material has the potential to render a more stable performance, in terms of that the fracture may not increase significantly with increasing current density. A property like this is believed by the author to help achieve a better durability of lithium ion batteries.

Assuming that the battery is being used to power a vehicle on the road, simulations under realistic driving conditions are also conducted in this work. The profile of current density drawn from the battery is scaled from three standard driving cycles: EPA 75, HWFET and US 06. A speed of 30 miles per hour is considered equivalent to 1C. Figures 26-28 record the voltage output and the dynamic fracture evolution during the three scaled cycles. EPA 75 represents the city driving condition and has more frequent stops and starts. Yet it results into the least, around 4% fracture, compared to the 6% under highway driving condition and 7% under US 06 cycle. Especially, it can be seen in Figure 26 that the fraction of damage remains constant during fluctuation of current density.

The fractures are more closely related to the highest current density. Among the three selected cycles, the highest C-rate is 2.5C in US 06 cycle, which represent an aggressive way of driving. The worst damage scenario is observed in US 06. These simulations under scaled realistic driving cycles indicate that the fracture damage is determined by the magnitude of current density and is less likely to be impacted by the frequently switching between high and low C-rates.
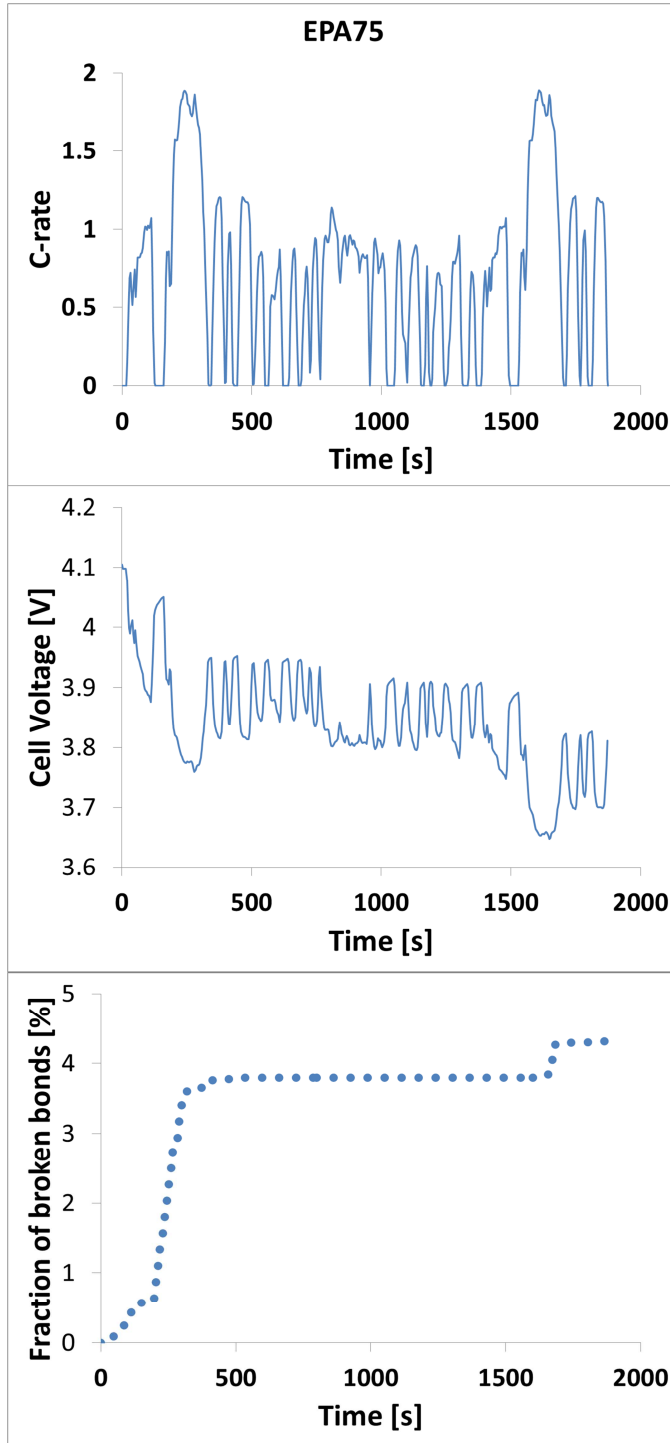
38

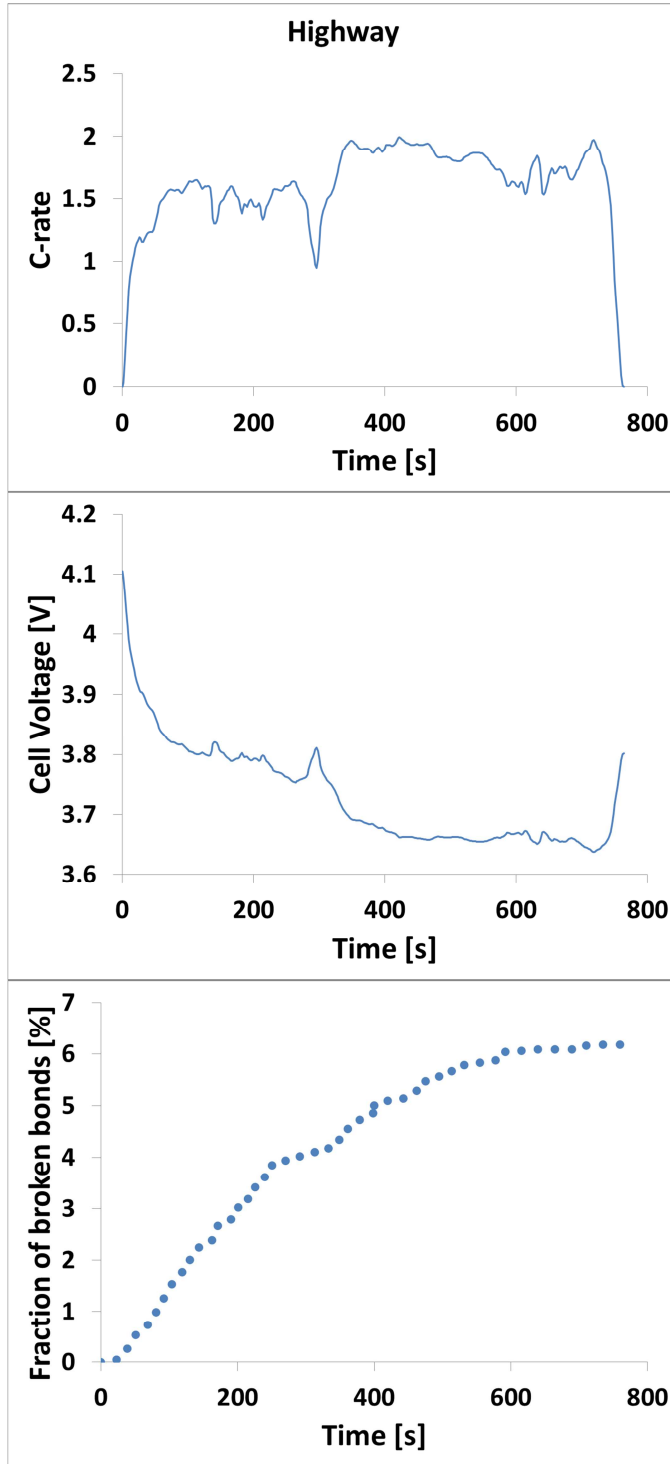**Figure 26 Scaled realistic driving cycle simulation: EPA75**

Figure 27 Scaled realistic driving cycle simulation: Highway
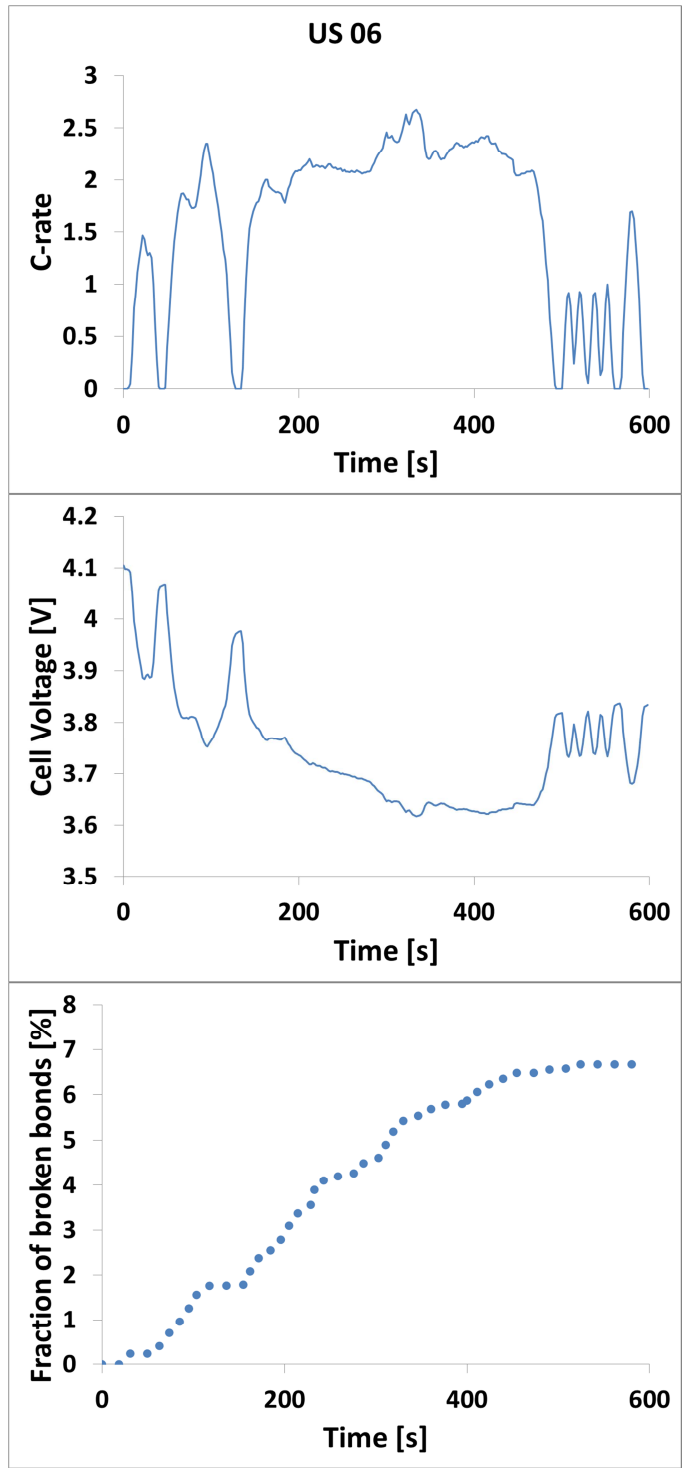
Figure 28 Scaled realistic driving cycle simulation: US06
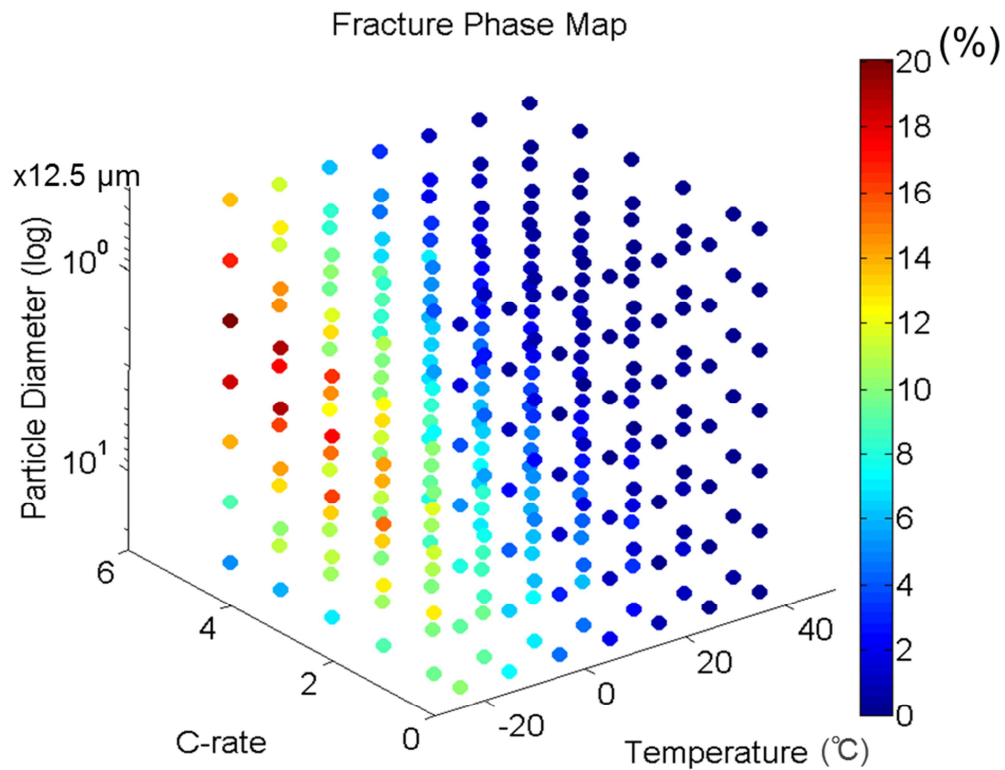
Figure 29 A 3D phase map to cover the effect of current density, particle size and temperature on fracture generation

A design map that predicts the damage under varying current density, particle size and operating temperatures is given in Figure 29. Generally, the fraction of broken bonds is proportional to current density and particle size, but negatively correlated to the ambient temperature. Yet, a critical value may present itself when the other two factors are fixed. For example, when discharging with 5C at -20°C, a particle of the size of R/16 would lead to the most severe damage inside the particle. Either a smaller or bigger particle would experience less fracture damage.

Summary

A single particle model of random lattice spring element coupled with solid phase lithium ion diffusion is extended to include active thermal effect. The heat generation and the effect of ambient temperature, current density and boundary condition on cell temperature are analyzed. Irreversible heat is found to be more dominating compared to the reversible heat. Lower ambient temperature and higher C-rate cause a higher cell temperature. At subzero temperatures, adiabatic condition can significantly boost the cell performances.

The diffusion induced damage is found to be positively related to current density and particle sizes. The monotonicity no longer exists at extremely low ambient temperature, where the diffusivity is particularly low. Dynamic evolution of fracture reveals a saturation phenomenon both during one single discharge process and a period of multiple discharge-charge cycles. The particle damage mostly happens during the first cycle.

A comparison between Si type and Graphite type materials shows that the former performs better at all temperatures. It leads to less damage and is less sensitive to current density. Simulations under realistic driving conditions show that the fraction of particle damage is determined by the highest current density drawn from the battery. Frequent shifting between high and low C-rates contributes little to the overall fracture generation or propagation.

CHAPTER III

IMPEDANCE ANALYSIS

Electrochemical impedance spectroscopy (EIS) is an ex-situ technique that measures the response of an electrochemical system to a small perturbing current or voltage. Since the perturbation is small, the response of the system is considered to be linear and the transfer function, or the ratio of the output to the input signal, shall be the same regardless of the type of applied signal. Based on this theory, any system can be characterized by its impedance, Z, which usually refers to the transfer function obtained in EIS measurement.
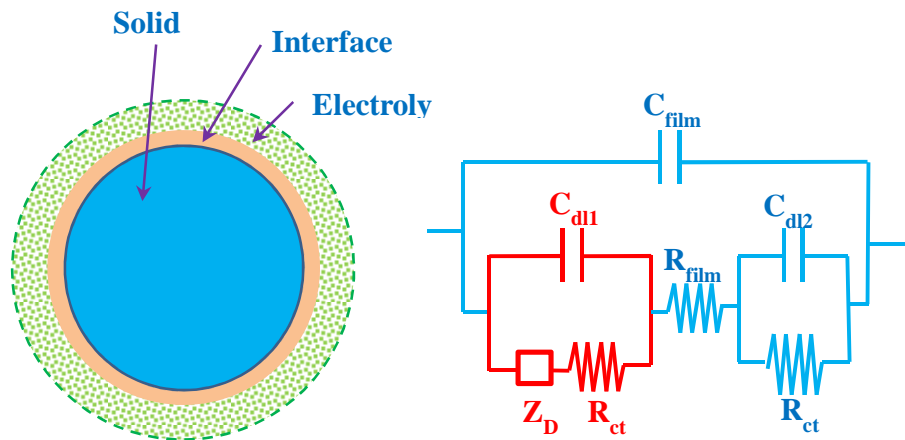

Figure 30 A schematic of impedance model of single electrode particle

Typically, the impedance Z consists of two parts, real part corresponding to the system response that is in-phase with the applied signal and imaginary part related to the system response that is out-of-phase with the perturbation. The impedance responses of

electrochemical systems have been traditionally modeled as a combination of some ideal

equivalent-circuit elements [32].

Mathematical Model

Figure 30 presents a schematic view of an impedance model of single electrode

particle. In this work, SEI effect is yet to be included and the interface film related terms

are thus ignored. Also, the diffusion and potential loss in electrolyte phase is not

considered here. Particular attention will be put onto the solid phase, which is shown in

red in the figure.

The following derivation is adjusted from the work of J. P. Meyers at al. [32]. By

considering the concentration change in the solid phase particle as a function of the

applied signal and frequency, the diffusion equation yields

$$j\omega\tilde{c}_s = \frac{D}{r^2}\frac{\partial}{\partial r}\left(r^2\frac{\partial c_s}{\partial r}\right) \tag{21}$$

The solution to the above differential equation is in the following form:

$$\tilde{c}_s = \frac{\tilde{i}_{n,faradaic}}{F}\left(\frac{R_s}{D}\right)\left(\frac{1}{\sinh\left(\sqrt{j\Omega_s}\right) - \sqrt{j\Omega_s}\cosh\sqrt{j\Omega_s}}\right)\frac{\sinh\left(\frac{r}{R_s}\sqrt{j\Omega_s}\right)}{\frac{r}{R_s}} \tag{22}$$

where $\Omega_s = \omega R_s^2/D_s$.

When $r = R_s$, one obtains the expression of surface concentration

$$\tilde{c}_{surf} = \frac{\tilde{i}_{n,faradaic}}{F}\left(\frac{R_s}{D}\right)\frac{\sinh\left(\sqrt{j\Omega_s}\right)}{\sinh\left(\sqrt{j\Omega_s}\right) - \sqrt{j\Omega_s}\cosh\sqrt{j\Omega_s}} \tag{23}$$

The transfer function is defined as

45

$$Y_s = -\frac{\tilde{i}_{n,faradaic} R_s}{FD\tilde{c}_{surf}} = \frac{\sqrt{j\Omega_s} - \tanh\left(\sqrt{j\Omega_s}\right)}{\tanh\left(\sqrt{j\Omega_s}\right)} \qquad (24)$$

At the particle surface, the faradaic current density is related to the potential drop across the interface by the Butler-Volmer equation

$$\tilde{i}_{n,faradaic} = i_{0,1}\left(\exp\left[\frac{\alpha_a F}{RT}\left(\tilde{\Phi}_1 - \tilde{\Phi}_2 - U\right)\right] - \exp\left[\frac{-\alpha_c F}{RT}\left(\tilde{\Phi}_1 - \tilde{\Phi}_2 - U\right)\right]\right) \qquad (25)$$

A linearization of Butler-Volmer equation yields

$$\tilde{i}_{n,faradaic} = \frac{i_{0,1}\left(\alpha_a + \alpha_c\right)F}{RT}\left[\tilde{\Phi}_1 - \tilde{\Phi}_{1f} - \left(-\frac{\partial U}{\partial c_s}\right)\tilde{c}_{surf}\right] \qquad (26)$$

With the following definition,

$$Z_{faradaic} = \frac{\tilde{\Phi}_1 - \tilde{\Phi}_{1f}}{\tilde{i}_{faradaic}} \qquad (27)$$

Eq. (22) can rearranged in the form of

$$Z_{faradaic} = R_{ct1} + Z_D \qquad (28)$$

where

$$R_{ct1} = \frac{RT}{i_{0,1}\left(\alpha_a + \alpha_c\right)F} \qquad (29)$$

$$Z_D = \frac{\left(-\frac{\partial U}{\partial c}\tilde{c}_{surf}\right)}{\tilde{i}_{faradaic}} \qquad (30)$$

Here, $\frac{\partial U}{\partial c_s}$ can be related to the first derivative of discharge or charge voltage curve. Combining Eq.(24) and Eq.(30) together, one gets

$$Z_D = \left(-\frac{\partial U}{\partial c}\right)\frac{R_s}{FD}\frac{\sqrt{j\Omega_s} - \tanh\left(\sqrt{j\Omega_s}\right)}{\tanh\left(\sqrt{j\Omega_s}\right)} \tag{31}$$

The open circuit potentials and the concentration profile of Lithium ions, with and without fracture effect, are obtained by the available single particle model described in chapter II. It can then be coupled with the above equations to calculate the impedance response of electrode particles with diffusion induced damage being taken into account.

Table 2 lists the parameters that are used in impedance calculation but not yet mentioned before.

Table 2 Input parameters in impedance simulation

Parameter	Value	Unit
C_{dl1}	10E-06 [27]	F/cm^2
$i_{0,1}$	0.69E-03 [27]	A/ cm^2
α_a	0.5	--
α_c	0.5	--

Results and Discussion

This work adopts the notation that Z' and Z'' represent the real and imaginary part of the complex impedance, respectively. In the following plots, the semi-circle is related to the R_{ct} and C_{dl1} terms and thus not the concern of this work. On the contrast, the slope of the line after the semi-circle is an indicator of the diffusivity in solid phase and the focus of this chapter. The steeper of the line's slope, the better the diffusivity. The impedance response of a spherical particle, with and without fracture effect, is shown in

47

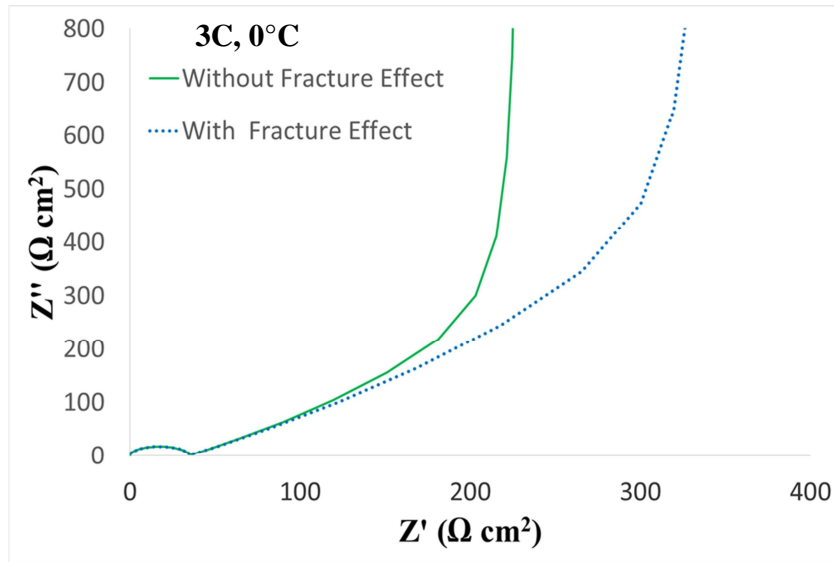Figure 31. As expected, the existence of crack and fracture increases the impedance response.

Figure 31 Comparison of impedance of spherical electrode particle: with and without fracture effect
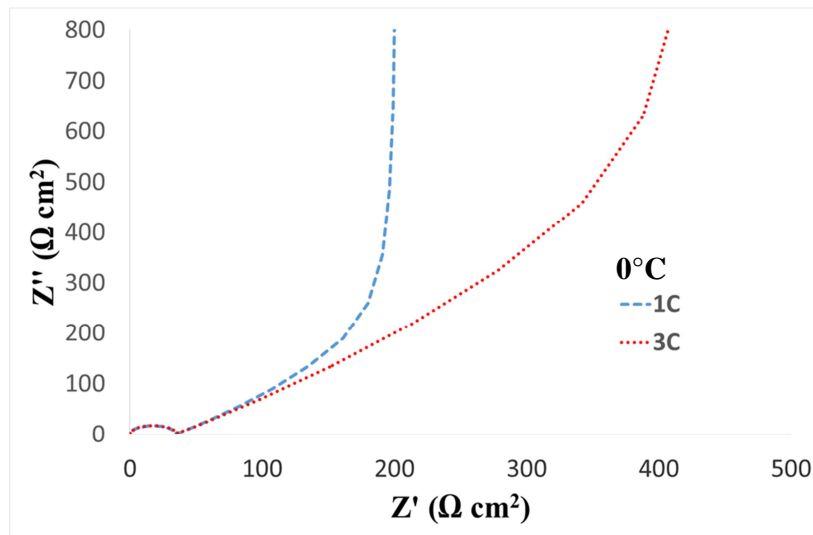

Figure 32 Comparison of impedance of spherical electrode particle: 1C and 3C

Figure 32 compares the impedance response with 1C and 3C at 0°C. The higher

C-rate, which leads to more fractures as discussed in chapter II, is confirmed to have

resulted to larger impedance. Figure 33 presents the impedance response of a spherical

particle at three different temperatures. The C-rate in this simulation is 2C. The

impedance response at -20°C is particularly larger and a possible explanation is that it

experiences more fracture damage and a consequently larger diffusion resistance.
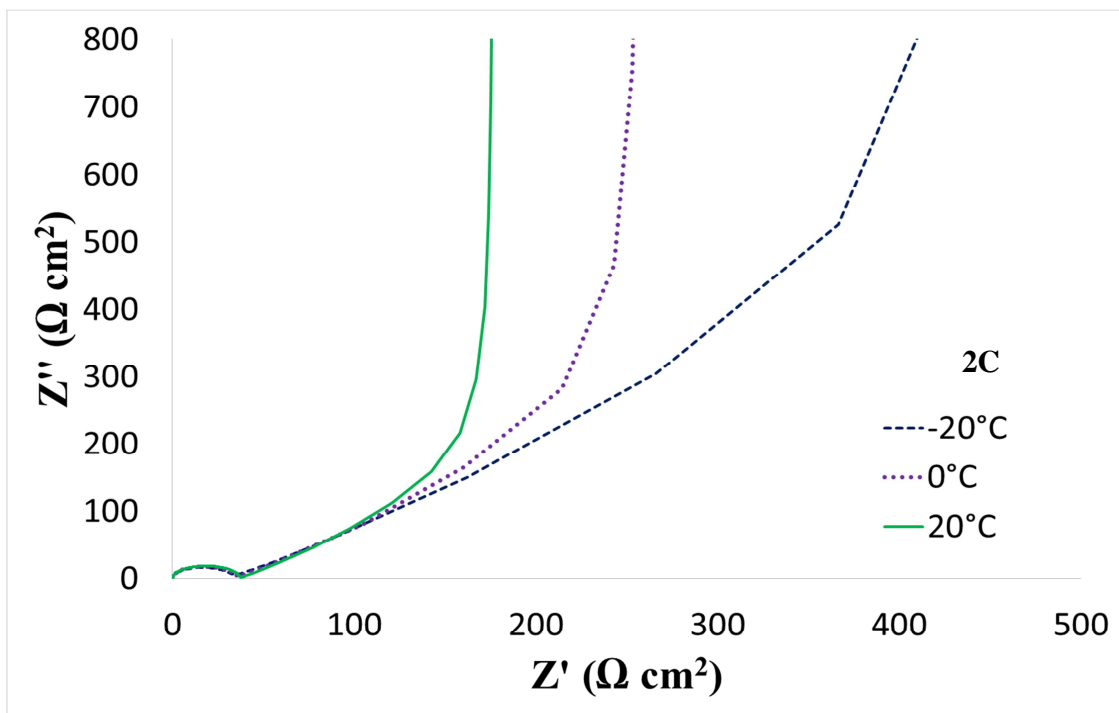

Figure 33 Temperature effect on impedance response of spherical particle

Figure 34 compares the calculated impedance for particles of different size.

Recall that in last chapter, smaller particle are proved to be desirable for their ability to

avoid fractures. One would expect to see that larger particles will be linked to impedance response of higher magnitude. This is the case as shown in the figure.
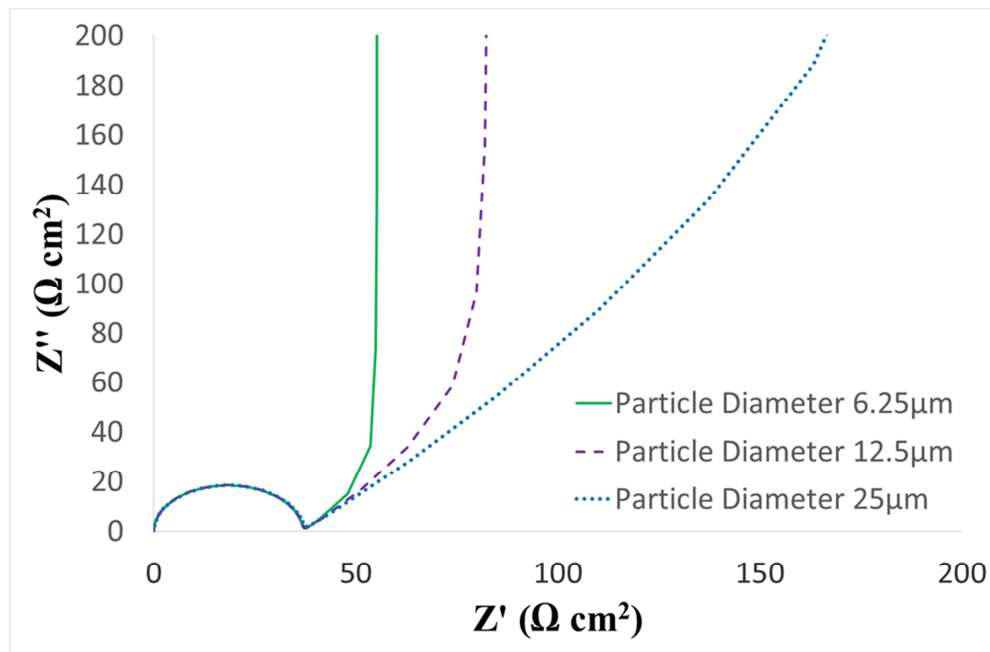

Figure 34 The impact of particle size on impedance response

Note in Figure 34 that the line for the particle with a diameter of 6.25µm has a nearly infinite slope. It nearly turns into a vertical line shortly after the semi-circle. This suggests a very large diffusion coefficient. As stated earlier, there is a critical size below which the particle is free of fracture damage. It seems that now there is a critical size below which the particle could enjoy extremely large diffusivity.

Simulations have also been conducted for a planar plate particle model. It was found that current density, temperature and particle size has similar effect on the impedance response of planar plate particles. By planar plate particle, this work refers to a rectangular domain with an aspect ratio of 3, as shown in Figure 35. Changing the size

50

of planar plate particle only changes the length but not the aspect ratio, the influence of which is yet to be determined.
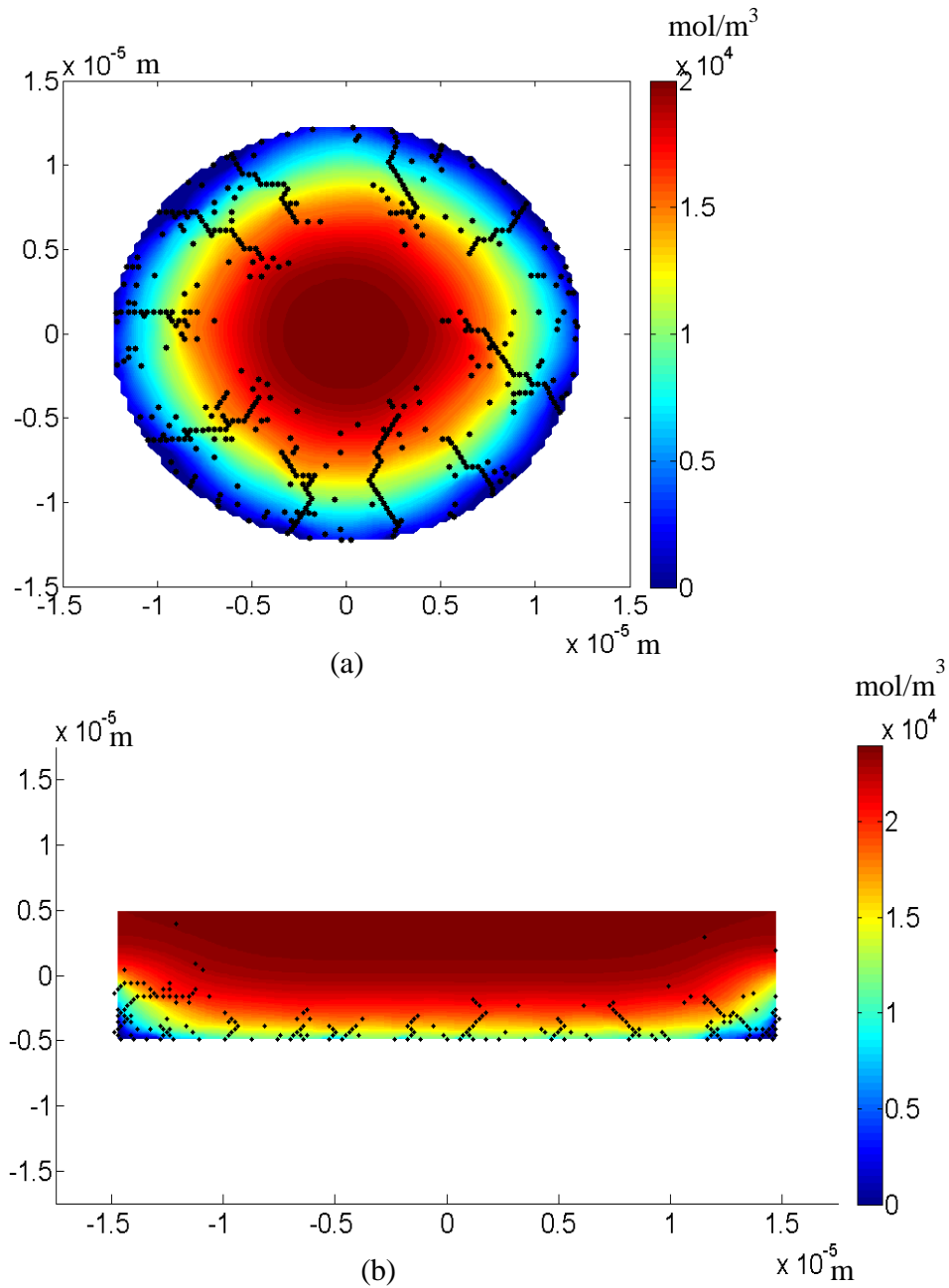

Figure 35 A contour plot with fractures for (a) spherical particle and (b) planar plate particle, 2C, 0°C
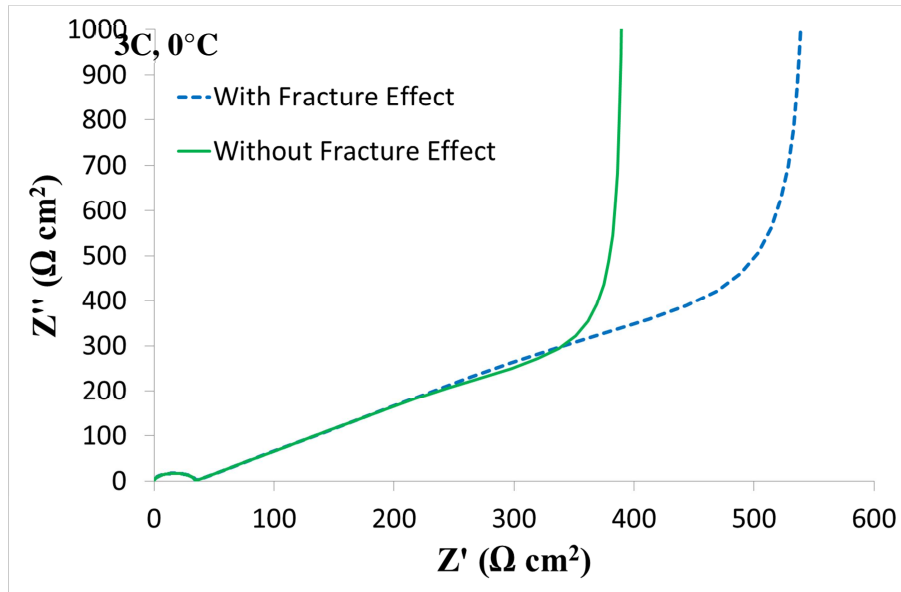
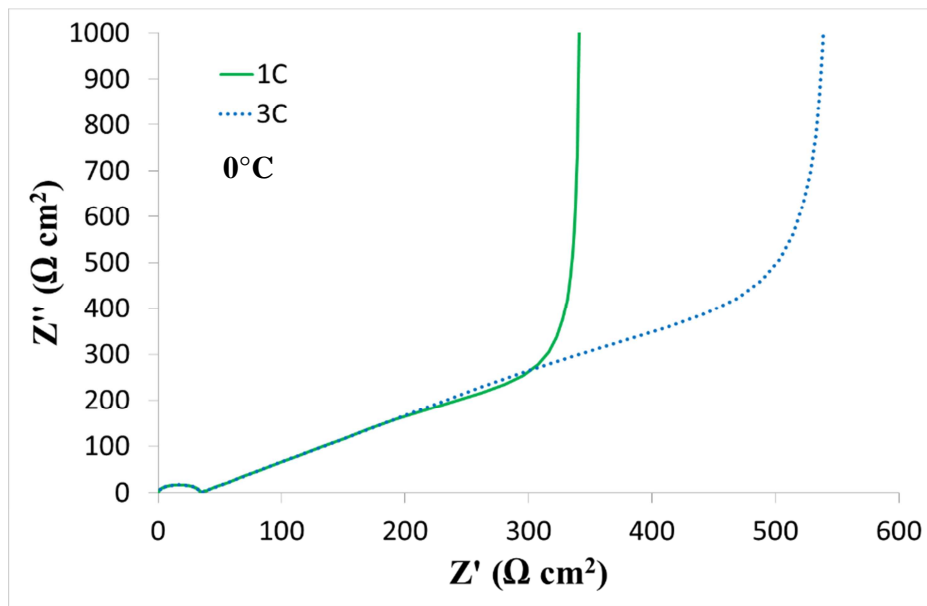**Figure 36 Comparison of impedance response of planar plate particle**

Figure 37 Impact of current density on impedance response of planar plate particle

For planar plate particles, the impedance response curve with fracture effect accounted is shifted to right, the larger zone, as can be seen in Figure 36. The input current density is 3C and the temperature is 0°C.

As expected, the planar plate particle also shows larger impedance at higher C-rate. Figure 37 provides a comparison of the response with 1C and 3C at 0°C. The impedance curve is shifted to right by more than 50%. It is worth mentioning here that the impedance results for 3C without fracture effect, presented in green in Figure 36, is nearly comparable with that of 1C with fracture effect included, shown in green in Figure 37. This means, the crack and fractures in electrode particle do contribute to the increase in impedance response, significantly. Depending on specific operating condition, its influence may be as considerable as that of current density. It is thus very important to control the fracture damage in order to avoid capacity loss, performance degradation or impedance rise.

The impacts of temperature and particle size are illustrated by Figures 38 and 39. The increase of impedance due to low temperature is still evident in planar plate particle simulations. On the other hand, similar particle size effect with that in spherical particles is also observed. Figure 39 shows the response curves for three different lengths of planar particle: L, L/2 an L/4, where L is 30 µm. When the particle size reduces to half, the calculated impedance is shown to be much lower. As the particle length is reduced, the response curve quickly turns into a vertical line. This tendency predicts a critical size below which the diffusion coefficient will be obtained as infinity.
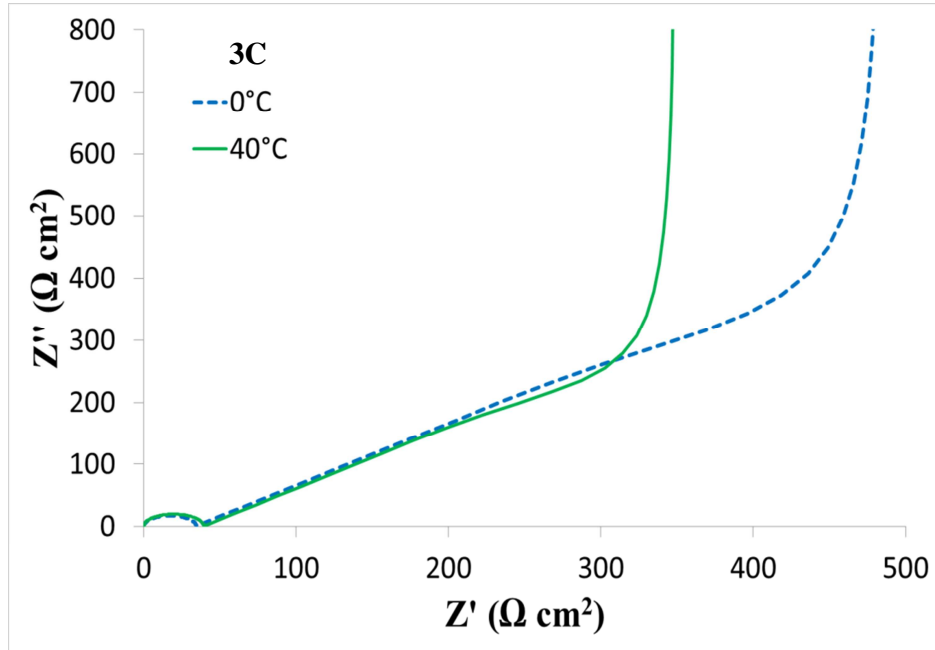
Figure 38 Temperature effect on impedance response of planar plate particle
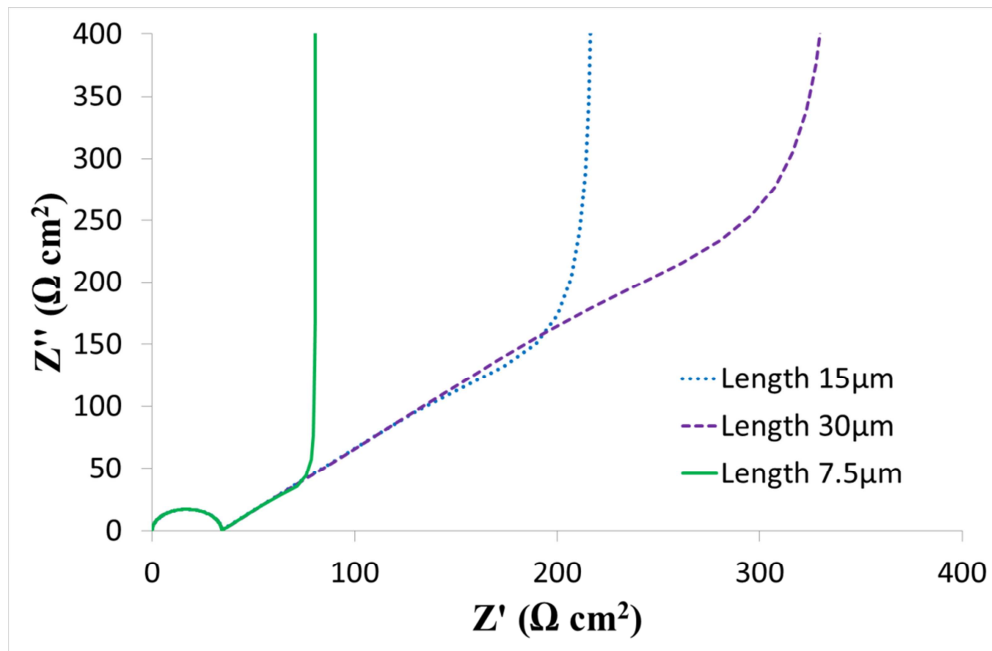
Figure 39 Particle size effect on impedance response of planar plate particle

54

Summary

This chapter made an attempt to gain an insight of how the fracture in electrode particle would affect its impedance response. Simulations were conducted on both spherical and planar plate particles. With fracture effect accounted, the impedance results are shown to be larger, indicating a smaller diffusivity. Similar findings are observed in both cases: the impedance response is directly related to current density, particle size but decreases with increasing temperature. The same thing is true for fracture damage as stated in last chapter. It is then reasonable to conclude that the existence of fracture does lead to impedance rise for electrode particles.

CHAPTER IV

CONCLUSION AND OUTLOOK

The energy and environment challenges have push the propulsion system of vehicles to higher efficiency and lower emissions. To this end, the electrification of vehicles calls for more powerful, more endure and more reliable lithium ion batteries as a powertrain solution. Several technical barriers, however, are yet to overcome for battery-powered electric vehicles to provide a satisfying driving range and to realize faster charging. Among those issues, diffusion induced stress is considered to cause fracture damage inside the battery electrodes, leading to permanent capacity loss. Although temperature greatly affects the voltage output and durability and safety, its impact on fracture generation is yet to be studied. This research work made an attempt to investigate the influence of temperature on fracture damage in lithium ion battery electrodes.

In this work, a single particle model of random lattice spring element is extended to include thermal effect. By coupling the heat conduction equation and upgrading the temperature-dependent parameters, the model successfully captures the temperature evolution inside the particle. With the predicted the temperature, the thermo-mechanical behavior is investigated with varying current density, ambient temperature and particle size. The impact of material property and realistic driving cycles are also taken into account. Results show that Si-type material has a greater potential than graphite type material to realize more durable batteries.

The fracture behavior is then related to the impedance response via a typical equivalent-circuit model. Impedance simulations are conduction for both spherical and planar plate particles. It is revealed that, for both type of particles, impedance response is directly related to current density and particle size but decreases with increasing temperature.

For future work, one idea is to further extend the current model to include the SEI film effect. The interface film has been drawing more and more attention and may have an influence on the mechanical behavior of battery electrodes. It is known that SEI film usually forms in first few cycles, which coincides with the formation of fractures. It is of great interest to identify the hidden link between SEI film and fracture damage.

Additionally, the impedance study in this work provides a perspective on how to experimentally verify some of the findings made in the presented simulations. Although EIS is an ex-situ measuring technique, it is still possible to gauge the fracture impact among all potential factors. In order to do that, a better understanding of the physical meanings of equivalent-circuit elements is required.

Ongoing work may also focus on different aspect ratio and micro-structures of electrode particles. In this work, the author maintains the same aspect ratio but only change the diameter for spherical particle or the length for planar plate particle when varying the particle size. Meanwhile, the impact of overlapping particles is also a topic that triggers our curiosity.

With further polishing efforts, the established model shall be able to shed more light on the thermo-mechanical behaviors of Lithium ion battery electrodes.

REFERENCES

[1] Standing Committee to Review the Research Program of the Partnership for a New Generation of Vehicles, Board on Energy and Environmental Systems, Transportation Research Board and National Research Council, Review of the Research Program of the Partnership for a New Generation of Vehicles: Seventh Report, National Academy Press, Washington, DC (2001)

[2] United States Council for Automotive Research LLC, Development of Advanced High-Performance Batteries for Electric Vehicle (EV) Applications, http://www.uscar.org/guest/publications.php, accessed on Sept. 22, 2013

[3] B. Scrosati, Journal of The Electrochemical Society 139 2776 (1992)

[4] M. B. Pinson and M. Z. Bazant, Journal of The Electrochemical Society, 160 (2) A243 (2013)

[5] Y. P. Wu, E. Rahm, and R. Holze, Journal of Power Sources 114(2) 228 (2003)

[6] M. L. Terranova, S. Orlanducci, E. Tamburri, V. Guglielmotti, and M. Rossi, Journal of Power Sources 246 (15) 167 (2014)

[7] V. Aravindan, J. Gnanaraj, Y. S. Lee, and S. Madhavi, J. Mater. Chen. A, 1, 3518 (2013)

[8] Y. Qi and S. J. Harris, Journal of The Electrochemical Society, 157 (6) A741 (2010)

[9] S. J. Harris, R. D. Deshpande, Y. Qi, I. Dutta, and Y. T. Cheng, Journal of Materials Research, 25(8), 1433 (2010).

[10] S. Huang, F. Fan, J. Li, S. Zhang, and T. Zhu, Acta Materialia, 61 4354 (2013)

[11] R. Deshpande, M. W. Verbrugee, Y. T. Cheng, J. Wang, and P. Liu, Journal of the Electrochemical Society, 159(10), A1730, (2012)

[12] D. Aurbach, E. Zinigrad, Y. Cohan and H. Teller. Solid State Ionics, 148 405 (2002)

[13] Q. Wang, P. Ping, X. Zhao, G. Chu, and J. Sun, Journal of Power Sources, 208 210 (2012)

58

[14] J. Christensen and J. Newman, Journal of Solid State Electrochemistry, 10, 293 (2006).

[15] J. Christensen and J. Newman, Journal of The Electrochemical Society, 153 (6) A1019 (2006)

[16] W. H. Woodford, Y. M. Chiang, and W. C. Carter, Journal of the Electrochemical Society, 157(10), A1052 (2010)

[17] S. Kalnaus, K. Rhodes, and C. Daniel, Journal of Power Sources, 196 8116 (2011)

[18] M. Zhu, J. Park, and A. M. Sastry, Journal of The Electrochemical Society, 159 (4) A492 (2012)

[19] X. Zhang, W. Shyy, and A. M. Sastry, Journal of the Electrochemical Society, 154(10), A910 (2007)

[20] X. Zhang, A. M. Sastry, and W. Shyy, Journal of The Electrochemical Society, 155 (7) A542 (2008)

[21] R. Fu, M. Xiao, and S. Y. Choe, Journal of Power Sources, 224 211 (2013)

[22] Y. F. Gao and M. Zhou, Journal of Power Sources, 230 176 (2013)

[23] T. M. Bandhauer, S. Garimella, and T. F. Fullerb, Journal of The Electrochemical Society, 158 (3) R1-R25 (2011)

[24] J. Newman and W. Tiedemann, Journal of The Electrochemical Society, 142 1054 (1995)

[25] W. B. Gu and C. Y. Wang, Journal of The Electrochemical Society, 147 (8) 2910 (2000)

[26] V. Srinivasan and C. Y. Wang, Journal of The Electrochemical Society, 150(1) A98 (2003)

[27] U. S. Kim, J. Yi, C. B. Shin, T. Han, and S. Park, Journal of The Electrochemical Society, 160 (6) A990 (2013)

[28] D. H. Jeon and S. M. Baek, Energy Conversion and Management, 52 2973 (2011)

[29] M. Guo, G. Sikha, and R. E. White, Journal of The Electrochemical Society, 158(2) A122 (2011)

[30] Y. Ji, Y. Zhang, and C. Y. Wang, Journal of The Electrochemical Society, 160 (4) A636 (2013)

[31] P. Barai and P. P. Mukherjee, Journal of The Electrochemical Society, 160 (6) A955 (2013)

[32] J. P. Meyers, M. Doyled, R. M. Darling, and J. Newman, Journal of The Electrochemical Society, 147 2930 (2000)

[33] M. D. Levi and D. Aurbach. J. Phys. Chem. B, 108, 11693 (2004)

[34] R.W.J.M. Huang, F. Chung, and E.M. Kelder., Journal of The Electrochemical Society, 153 A1459 (2006)

[35] S. Sunde, I. A. Lervik, L-E Owe, and M. Tsypkin, Journal of The Electrochemical Society, 156, B927 (2009)

[36] A. Jossen. Journal of Power Sources, 154 530 (2006)

[37] D. Andre, M. Meiler, K. Steiner, Ch. Wimmer, T. Soczka-Guth, and D.U. Sauer. Journal of Power Sources, 196 5334 (2011)

[38] P. P. Mukherjee, S. Pannala, and J. A. Turner. Modeling and Simulation of Battery Systems. In Handbook of Battery Materials, 2nd ed.; Daniel, C., Besenhard, J. O., Eds.; Wiley-VCH Verlag GmbH &Co. KGaA: Weinheim, 843 (2011)

[39] Y. T. Cheng and M. W. Verbrugee, Electrochemical and Solid State Letters, 13, A128 (2010)

[40] R. Grantab and V. B. Shenoy, Journal of The Electrochemical Society, 158(8), A948 (2011)

[41] M. Sakai, K. Urashima, and M. Inagaki, Journal of American ceramics Society, 66(12), 868 (2013)

[42] G. Y. Gu, S. Bouvier, C. Wu, R. Laura, M. Rzeznik, and K.M Abraham, Electrochimica Acta 45 3127 (2000)

[43] C. W. Park and A. K. Jaura, SAE 2003-01-2286.

[44] S. Santhanagopalan, Q. Guo, P. Ramadass, and R. E. White, Journal of Power Sources 156 620 (2006)

[45] T. Kulova, A. Skundin, E. Nizhnikovskii, and A. Fesenko, Russian Journal of Electrochemistry, 42, 259 (2006).

[46] K. Nakamura, H. Ohnoa, K. Okamurac, Y. Michihiroa, I. Nakabayashib, and T. Kanashiro, Solid State Ionics, 135, 143 (2000)

[47] O. Y. Egorkina and A. Skundin, Journal of Solid State Electrochemistry, 2, 216 (1998).

[48] H. Zheng, J. Qin, Y. Zhao, T. Abe, and Z. Ogumi, Solid State Ionics, 176, 2219 (2005)

[49] K. Kumaresan, G. Sikha, and R. E. White, Journal of The Electrochemical Society, 155 (2) A164 (2008)

[50] Y. T. Cheng and M. W. Verbrugee, Journal of the Applied Physics, 104, 083521, (2008)

[51] R. Deshpande, Y. T. Cheng, and M. W. Verbrugee, Journal of Power Sources, 195(15), 5081 (2010)

[52] R. T. Purkayastha and R. M. McMeeking, Computational Mechanics, 50(2), 209 (2012)

[53] R. Deshpande, Y. Qi, and Y. T. Cheng, Journal of the Electrochemical Society, 157(8), A967, (2010)